JOURNAL OF GEOPHYSICAL RESEARCH, VOL. 106, NO. B8, PAGES 16,075–16,099, AUGUST 10, 2001

High-resolution bathymetric surveys using scanning sonars: Lava flow morphology, hydrothermal vents, and geologic structure at recent eruption sites on the Juan de Fuca Ridge

William W. Chadwick Jr.,[1] Daniel S. Scheirer,[2] Robert W. Embley,[1] and H. Paul Johnson[3]

Abstract. The CoAxial and Cleft segments of the Juan de Fuca Ridge have isolated, chronic, high-temperature, and focused hydrothermal vent sites. Both segments also have experienced recent volcanic eruptions which produced extensive, ephemeral, low-temperature, and diffuse hydrothermal venting. To study the geologic setting of these sites, high-resolution bathymetric surveys at eight locations on the CoAxial and Cleft segments were collected between 1993 and 1999. Two 675-kHz scanning sonar systems were used, Mesotech on the submersible *Alvin* and Imagenex on the remotely operated vehicle *Jason*. The bathymetry from these surveys can be gridded at a scale of 2–4 m and contoured at 1 m and thus can resolve many fine-scale features on the seafloor that are indistinguishable in multibeam bathymetry collected at the sea surface. Bathymetric data at this resolution are particularly useful for identifying geologic features related to diking, faulting, and lava flow emplacement. For example, the high-resolution bathymetric maps show that submarine fissure eruptions that form pillow lavas last long enough to become localized and to produce point source constructs along their length, and their extrusion rate is low enough that no significant drainback occurs. In contrast, lobate sheet flows are formed by short-lived, high-effusion rate eruptions in which no localization of output occurs along the eruptive fissure, and inflation is quickly followed by drainback, resulting in extensive collapse features. However, if the process of submarine lava flow inflation occurs at a slower rate and over a longer period of time, it can create lava rises up to 25 m high with distinctive structure and morphology. The scanning sonar data also show that fissures and grabens have formed or reactivated where dikes approach the surface adjacent to recent eruptive sites. The fine-scale bathymetry establishes that all the hydrothermal vent sites studied at the CoAxial and Cleft segments are located along prominent volcanic or tectonic extensional structures which provide the physical pathway for fluids from the subsurface to the seafloor. Furthermore, the fine-scale morphology of recent lava flows can be used as a qualitative indication of eruption duration.

1. Introduction

Modern bathymetric mapping of the deep ocean floor is typically accomplished by multibeam sonar systems that are mounted on the hull of a ship. These systems have an inherent limitation in resolution in deep water since the acoustic source is at the ocean surface and the sound must traverse the entire water column twice. At mid-ocean ridge depths of 2000–3000 m, each acoustic beam from a multibeam system integrates sonar returns from a patch of seafloor 30–100 m in diameter. Therefore features at this scale or below cannot be resolved in multibeam bathymetry. On the other hand, near-bottom visual observations of the seafloor from submersibles such as remotely operated vehicles (ROV) or manned submarines are at a scale <10 m, the maximum distance that lights illuminate, along seafloor traverses. Consequently, there is a gap between the scale of near-bottom observations and the resolution of surface-based mapping systems. Unfortunately, there are many im-

[1]Hatfield Marine Science Center, Oregon State University/NOAA, Newport, Oregon.
[2]Department of Geological Sciences, Brown University, Providence, Rhode Island.
[3]School of Oceanography, University of Washington, Seattle, Washington.

Paper number 2001JB000297.
0148-0227/01/2001JB000297$09.00

portant volcanic and tectonic features on the seafloor that fall within this gap.

To bridge this resolution gap, we must utilize sonar mapping systems that can collect data closer to the seafloor. One such system is the DSL-120, a sonar system which is towed ~100 m above the seafloor and provides detailed seafloor backscatter and less detailed bathymetry data [*Scheirer et al.*, 2000]. The bathymetry for DSL-120 is based on a phase-difference calculation of sonar signals returning to paired transducers. Bathymetry based on this calculation is more prone to uncertainty than that based on direct measures of sonar return times; these more direct measures are provided by sonars which scan beneath the submersible, transmitting and receiving a high-frequency pulse which returns from the seafloor at a known angle. Mesotech and Imagenex scanning sonars are two such high-frequency, short-range sonar systems capable of collecting high-resolution bathymetric data in the deep ocean when mounted on a submersible. Bathymetry generated from scanning sonar data can resolve seafloor features that are a few meters across, over distances of hundreds to thousands of meters. These bathymetric maps can then be used to interpret the geology and structure of the seafloor, to refine interpretation based on multibeam sonar maps, and to provide a larger context for near-bottom visual observation and sampling programs. This intermediate-scale bathymetry reveals spatial and morphologic relationships between features on the seafloor that would otherwise not be discernible, and it allows the fine-scale morphology of hydrothermal vent or volcanic eruption sites to be mapped and studied in detail. Another use of these data is for calculating terrain corrections to remove the effect of bathymetry from near-bottom gravity and magnetic measurements [*Tivey and Johnson*, 1995; *Tivey et al.*, 1997; *Pruis and Johnson*, 1998; *Gilbert and Johnson*, 1999]. Scanning sonar surveys also serve as detailed topographic baselines to which future surveys could be compared to detect and quantify depth changes on the seafloor due to volcanic or tectonic events, similar to the way in which changes have been documented by repeated multibeam surveys [*Fox et al.*, 1992; *Chadwick et al.*, 1995, 1998; *Embley et al.*, 1999] but at a much higher resolution.

Previously, *Kurras et al.* [1998] constructed maps of two frequently visited sites within the axial summit trough on the East Pacific Rise at 9° 49′–51′N, using data from a Mesotech sonar collected during 23 *Alvin* dives over 5 years. None of these *Alvin* dives was specifically devoted to sonar mapping, however, so the spatial coverage was somewhat limited. At the Endeavour segment of the Juan de Fuca Ridge, an Imagenex sonar on *Jason* was used to make a three-dimensional map of a hydrothermal chimney field [*Delaney et al.*, 2001]. More recently, the Autonomous Benthic Explorer (ABE) vehicle mapped sites on the southern East Pacific Rise at 17° 28′S with an Imagenex sonar, revealing lava channels descending down the flanks of the ridge axis [*Bradley et al.*, 1999; *Cormier et al.*, 1999; *Ryan et al.*, 1999]. *Singh et al.* [2000] described how an archeological site was mapped in the Mediterranean using the Imagenex sonar on *Jason*.

In this paper, we describe the methods we have used to collect and process scanning sonar data in order to create high-resolution bathymetric maps. We present results from eight surveys between 1993 and 1999 at selected sites on the Juan de Fuca Ridge (Figures 1 and 2) with the Mesotech sonar mounted on *Alvin* and the Imagenex sonar mounted on *Jason*. Both sensors are part of the National Deep Submergence Facility at the Woods Hole Oceanographic Institution. Bathymetry from two of the eight surveys (Plates 1 and 2 and Figure 3) was previously published by *Chadwick and Embley* [1998] but is included here because the surveys show how high-resolution data can contribute to the geologic interpretation of seafloor structures.

2. Instrumentation, Survey Methods, and Data Processing

2.1. Instrumentation

The Mesotech and Imagenex sonars used in this study are both "pencil beam" scanning sonars that transmit a narrow (1.7°), high-frequency acoustic pulse at 675 kHz, providing a maximum range of ~100 m. Both sonars operate in either a backscatter or profile mode; the former mode records acoustic amplitudes continuously between outgoing pings, whereas the latter records a single bottom return from each ping. All the data in this paper were collected in profile mode. In this mode the sonar head is pointed downward and mechanically rotates back and forth through a specified angle sector while collecting discrete acoustic ranges to the seafloor. As the submersible moves forward and the sonar head sweeps from side to side perpendicular to the vehicle's track, depth soundings are collected in a zig-zag pattern on the seafloor (Plate 1a).

2.2. Survey Methods

Designing a scanning sonar survey requires careful consideration of a variety of parameters related to both sensor settings and the vehicle path over the seafloor; in most cases, there are trade-offs in these considerations. The description below relates our experiences from field programs on the Juan de Fuca Ridge over the past decade. We used the scanning sonars to collect bathymetry over areas of interest by having a submersible drive a series of evenly spaced, parallel track lines. Generally, the surveys are hundreds to thousands of meters on a side with areas that range from 1×10^5 m^2 up to 2×10^6 m^2. Several important survey parameters are specified directly on the sonar control panel, including range, gain, sector size, and scanning speed. The scanning speed controls the size of the step angle between sonar pings and therefore the number

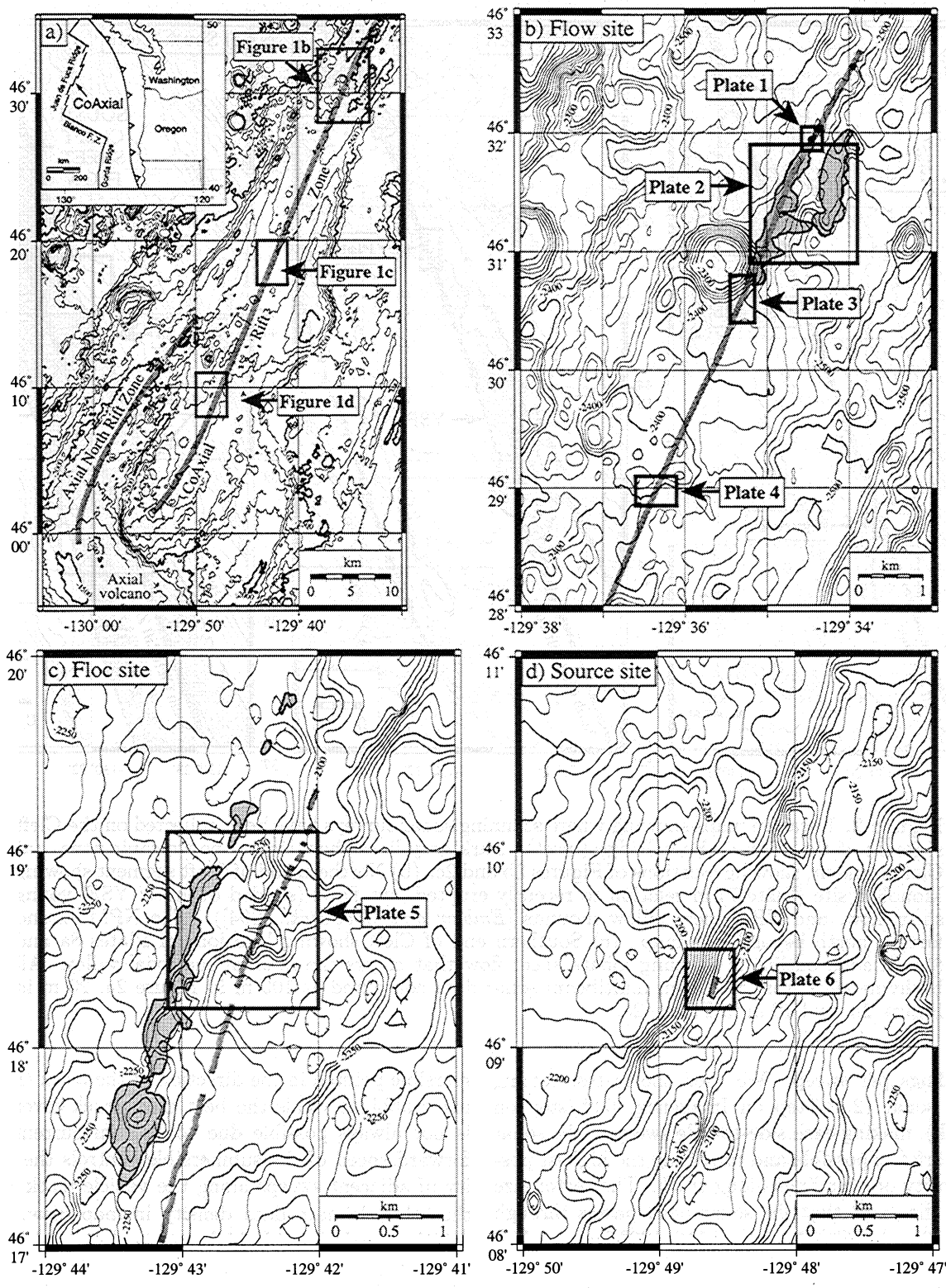

Figure 1. Location maps showing where high-resolution bathymetric surveys have been collected at the CoAxial segment on the central Juan de Fuca Ridge (inset). (a) CoAxial segment, showing locations of Figures 1b, 1c, and 1d. Dark shaded lines show axis of neovolcanic zone along Axial north rift zone and the CoAxial segment. (b) Flow site, showing the locations of Plates 1, 2, 3, and 4 in relation to recent lava flows (shaded outlines). Dark shaded line shows path of 1993 dike intrusion that fed the western of the two lava flows. This path was marked by hydrothermal activity along the crest of the 1993 pillow mound and from fissures and grabens off the flow immediately after the event. (c) Floc site, showing location of Plate 5 in relation to recent lava flows (shaded outlines) and a reactivated fissure/graben system that was hydrothermally active after the 1993 dike intrusion (dark shaded lines). (d) Source site, showing location of Plate 6 and high-temperature vents (dark shaded line). All bathymetry is from SeaBeam multibeam sonar data contoured at 100 m in Figure 1a, 20 m in Figure 1b, and 10 m in Figures 1c and 1d.

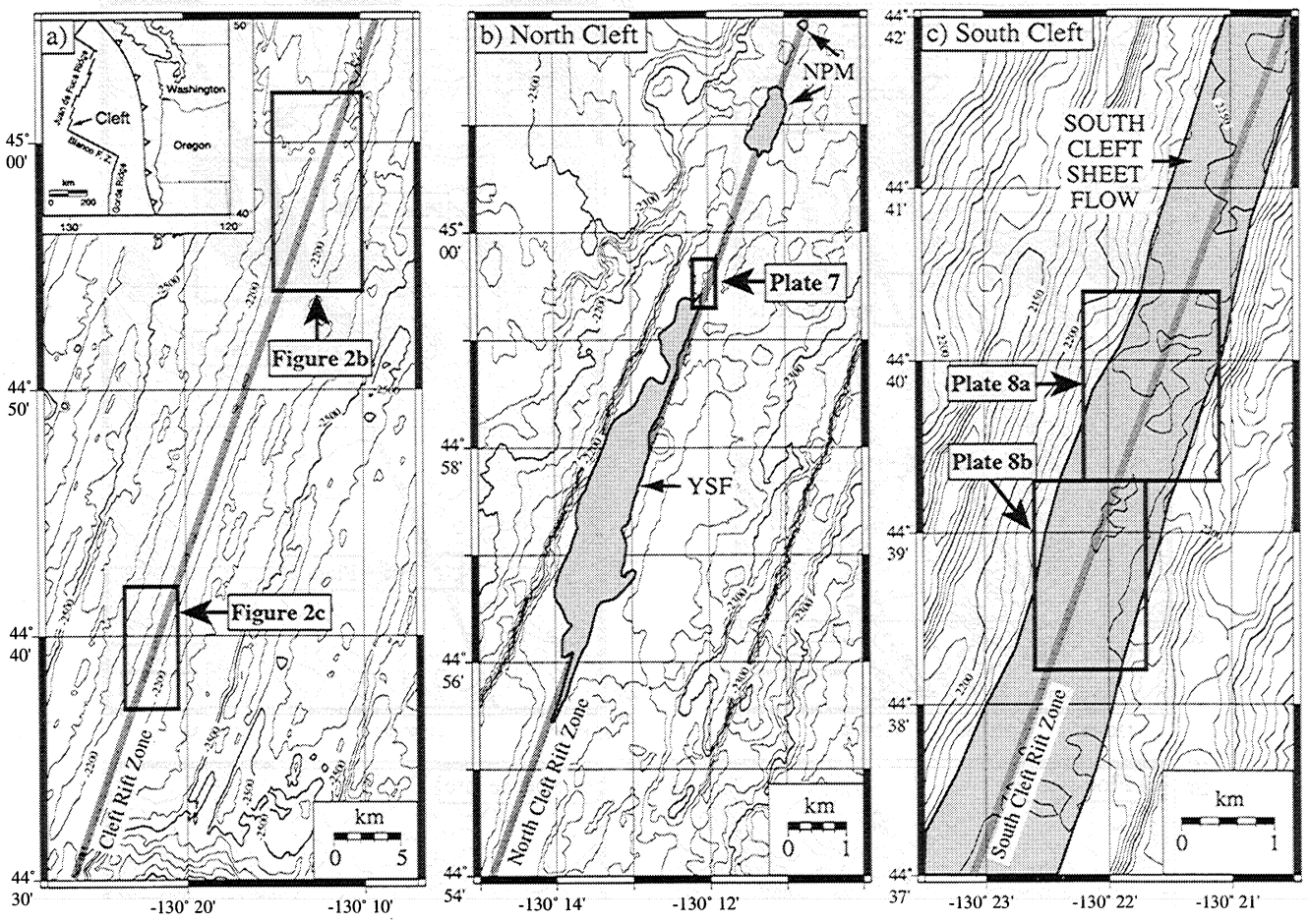

Figure 2. Location maps showing where scanning sonar surveys have been collected on the Cleft segment of the Juan de Fuca Ridge (inset). Dark gray lines show axis of neovolcanic zone. (a) Cleft segment, showing locations of Figures 2b and 2c. (b) Northern end of Cleft segment showing Monolith site (Plate 7) in relation to recently erupted lava flows (shaded outlines; YSF, young sheet flow, and NPM, new pillow mounds [*Embley and Chadwick*, 1994]). The NPM extend farther north beyond this map. (c) Southern end of Cleft showing locations of Plates 8a and 8b. Shaded outline is a young lobate sheet flow that covers the floor of the axial valley. All bathymetry is from SeaBeam multibeam sonar data contoured at 100 m in Figure 2a, 20 m in Figure 2b, and 10 m in Figure 2c.

of soundings per sweep. We used the fastest setting on each sonar (2.4°/step on Imagenex; 0.9°/step on Mesotech), making each side-to-side sweep of the sonar head as brief as possible and providing the highest possible density of soundings along track. The sector size controls the angle that the sonar head passes through for each sweep, and we have used 110–120° for mapping. The maximum range setting controls how long the sonar waits for the return echo between outgoing pings. With a 120° sector size, we used a maximum range that was twice the vehicle altitude. The gain can be varied to maximize the signal to noise ratio. These parameters are set before a survey begins and are changed during a survey only if necessary.

During a survey, data were usually collected at an altitude of 25 m, providing coverage over a ~70–80 m wide swath. Survey track lines were spaced 60 m apart to provide a small amount of overlap. Having the submersible pointed in the direction of the track (minimizing crabbing) yields the best cross-track coverage but is not always possible due to bottom currents. The forward speed of the submersible controls the proximity of adjacent sweeps along the vehicle track line and thus the ultimate data density in map view. Slower vehicle speeds provide higher data density, but higher speeds provide greater spatial coverage within a given time period. We have found a forward speed of 0.5 knots (~15 m/min) is a good compromise. *Alvin* and *Jason* navigation is typically based on the acoustic travel times from a long-baseline net of transponders that are moored 100–200 m above the bottom, providing several position fixes per minute. Continuous and consistent navigation of the submersible is critical to the quality of the final bathymetry map. For this reason, vehicle track lines that are long and straight and run at a constant speed are best, so that interpolation

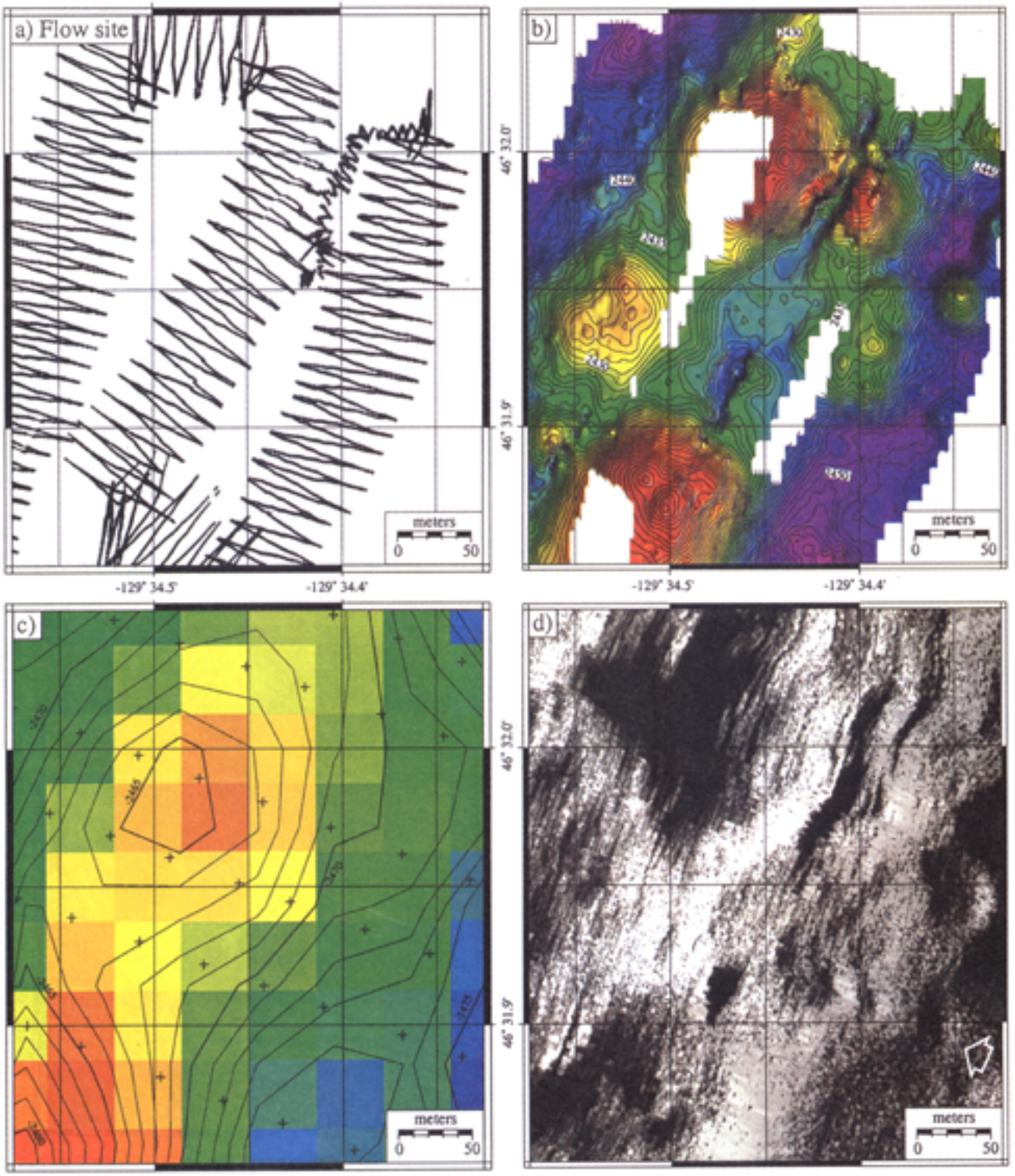

Plate 1. Maps of a small area at the northern end of the 1993 lava flow at the CoAxial Flow site where a small satellite flow erupted out of a graben (location shown in Figure 1b). (a) Map of individual Mesotech sonar soundings from *Alvin* dive 2792 (25296 soundings in all, shown by pluses, collected in 3 hours). The zig-zag pattern was produced by the sonar head moving from side to side as the submersible moved forward at ~25-m altitude, then at 10-m altitude producing tighter pattern in upper right. (b) High-resolution bathymetry (4-m grid cell size; 20-m interpolation radius; 1-m depth contours) from the soundings shown in Plate 1a. (c) Bathymetry of same area from SeaBeam multibeam sonar for comparison with Plate 1b (50-m grid cell size; 1-m contours). The grid was made from only 38 soundings, shown by pluses. SeaBeam depths based on an uncorrected sound speed. (d) AMS-60 sidescan sonar image independently verifies features shown in the Mesotech bathymetry in Plate 1b; the graben north of the main 1993 lava flow stands out in acoustic shadow, except where small satellite lava flows have overflowed and buried it (1-m grid cell size; arrow shows insonification direction; white is high reflectivity, black is acoustic shadow). After Plate 1 of *Chadwick and Embley* [1998].

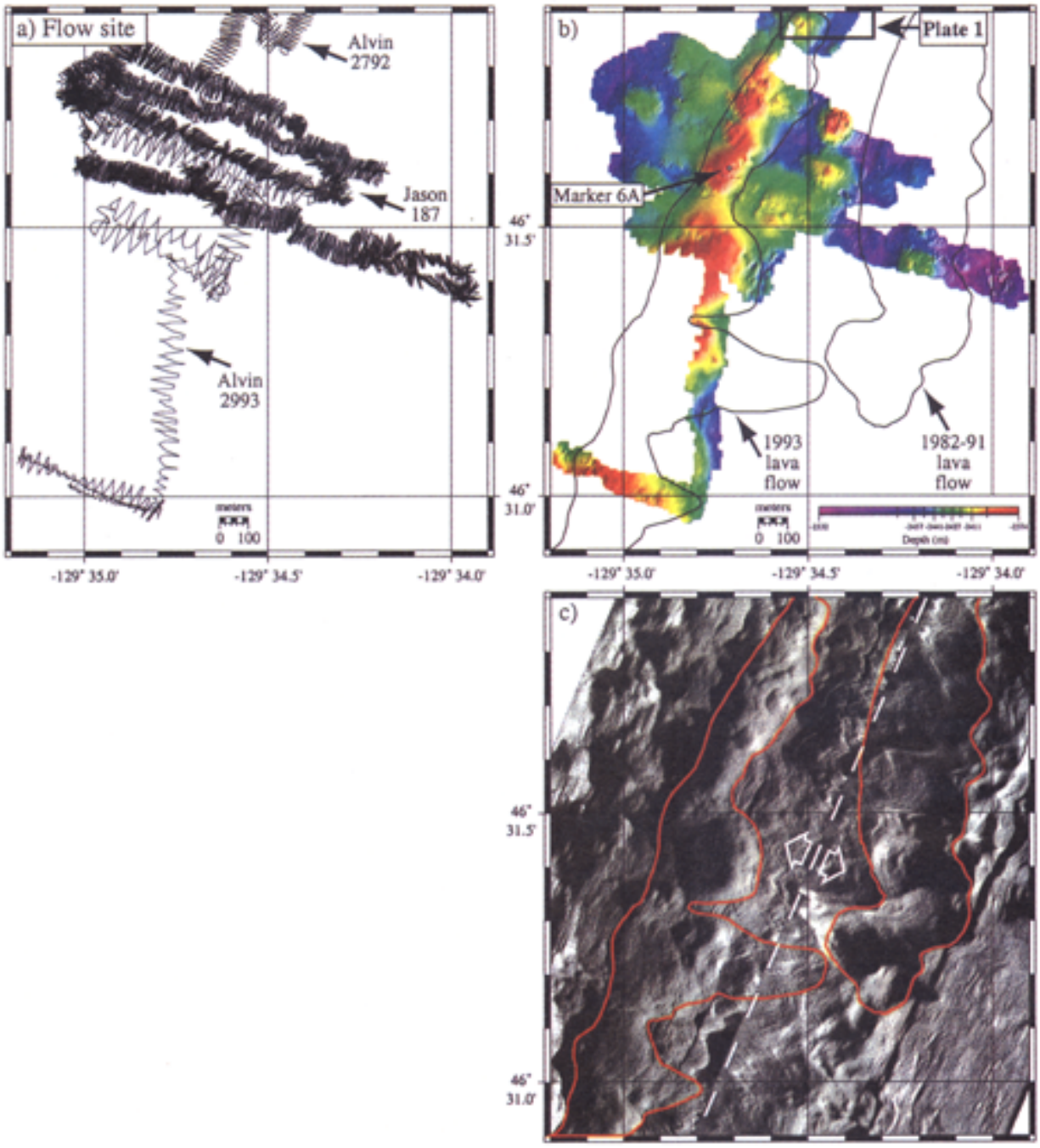

Plate 2. Maps of the middle part of the 1993 lava flow at the CoAxial Flow site (location shown in Figure 1b). (a) Pattern of soundings from Mesotech and Imagenex surveys used to make map in Plate 2b. Note the Imagenex data from *Jason* dive 187 is much denser than the Mesotech data from *Alvin* dives 2792 and 2993 because the sonar head of the Imagenex can move at a faster rate from side to side. (b) Bathymetric map from the soundings in Plate 2a (4-m grid cell size; 40-m interpolation radius). (c) AMS-60 side-scan sonar image of the same area, showing correspondence to features in Plate 2b (4-m grid cell size; dashed line shows side-scan towfish track; arrows show insonification direction; white is high reflectivity, black is acoustic shadow).

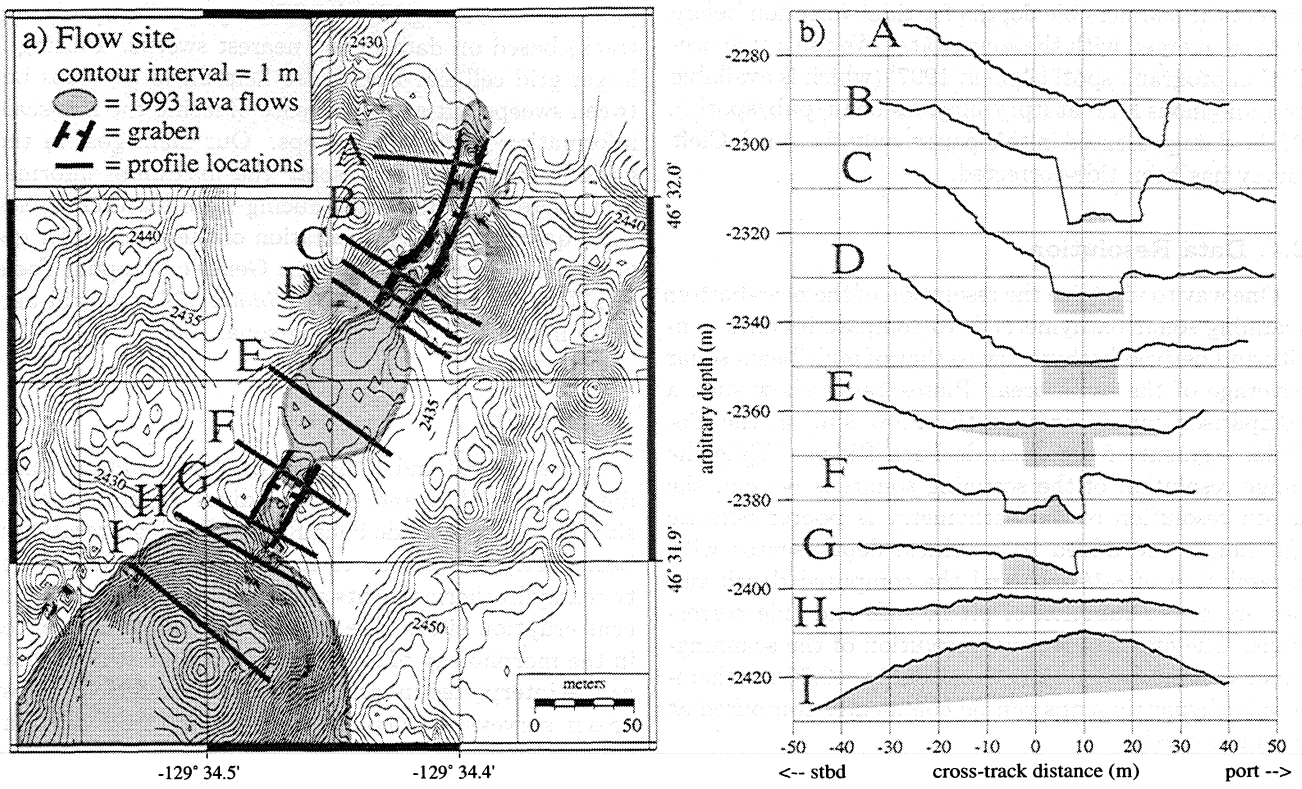

Figure 3. (a) Interpretive geologic map of same area as shown in Plate 1 showing 1993 lava and graben structures. Lines labeled A–I are locations of individual Mesotech depth profiles shown in Figure 3b. (b) Individual depth profiles (locations shown in Figure 3a) offset from one another by an arbitrary depth for clarity. Shaded areas show interpreted extent of 1993 lava below each profile. After Plate 1 of *Chadwick and Embley* [1998].

can be used to fill any small gaps in navigation. For surveys collected over several years in the same area but using different transponder nets, a small navigational shift may be required to register one survey to another based on position fixes at known bottom marker sites. Long-lived transponder networks are best for multiyear surveys.

2.3. Data Processing

Three distinct sets of data are required for making a bathymetry map from scanning sonar data: the sonar data itself, submersible navigation, and attitude data from the submersible (depth, heading, pitch, and roll). All the data presented in this paper were processed with two programs written by D. Scheirer, bin_dsl_data and scanning_sonar (which are available by FTP at http://www.geo.brown.edu / grads / scheirer / programs.html). First, the navigation data must be edited to eliminate bad fixes. Then, using bin_dsl_data, the navigation is interpolated and combined with the vehicle attitude data into a merge file with a common time base (a 1-s interval works well for our purposes). The merge file, sonar file, and sensor mount offsets are processed together to geometrically locate the position of every sonar ping on the seafloor using scanning_sonar. The scanning_sonar program can also perform a variety of simple beam editing functions to help remove bad soundings in the dataset. Other graphical editing software can be used to clean up scanning sonar data on a profile by profile basis, but this is more time consuming. The output from scanning_sonar is a file of longitude-latitude-depth (or X–Y-depth) triples which can then be gridded to construct bathymetric maps.

Alternatively, cross-track depth profiles can be output to create high-resolution cross sections of specific seafloor structures (Figure 3b). Although the emphasis in this paper is on map views of bathymetry, the finest-scale information is available by examining individual profiles; gridded versions of the data require some amount of averaging and interpolation. Depth profiles are also very useful for initially determining the quality of the sonar data and for ensuring that bad soundings are completely removed from the data before gridding.

Our pre-1998 surveys were relatively short, and we did not account for the effects of tides on the derived bathymetry because this correction did not appear to be necessary. Since 1998, however, we have found that it is also useful to make a tidal correction to submersible depth when combining data from dives on different days or years because apparent depth offsets can appear in data collected at different parts of the tidal cycle (up to ±1 m on the Juan de Fuca Ridge). We now routinely

correct the submersible depths for tidal variation before they are merged with the sonar data. We use a tide prediction program, spotl [*Agnew*, 1997] (which is available by anonymous FTP at ftp://bilby.ucsd.edu/pub/spotl/). Of the data presented in this paper, only the south Cleft survey has been tide-corrected.

2.4. Data Resolution

One way to visualize the resolution of the near-bottom scanning sonar bathymetry is to compare its data density and derived bathymetry to that of multibeam sonar coverage of the same area. Plates 1a–1c show such a comparison for an area at the Flow site on the CoAxial segment of the Juan de Fuca Ridge. While the range resolution of the scanning sonars is ~1 cm, the depth resolution of the bathymetry is poorer because the ranges are added to a vehicle depth sensor with a resolution of ~10 cm, and the computed depth values are also a function of pitch, roll, and tide corrections. The effective vertical resolution of the scanning-sonar-derived bathymetry is probably <0.25 m; therefore bathymetric maps can be confidently contoured at a 1-m interval.

In map view, one important constraint on the horizontal resolution of the sonar data is the quality of the vehicle position data, which for long-baseline acoustic navigation is typically 2–5 m [*Fornari et al.*, 1998; *Lerner et al.*, 1999]. The horizontal resolution is also a function of the data density. The zig-zag distribution of soundings on the seafloor is inherently uneven; the sonar data are much denser across track (0.5–1 m) than along track (5–20 m). The distribution of soundings depends on the type of sonar used and how each survey is conducted. For example, the difference in the maximum speed that the sonar head can sweep from side to side between the Mesotech and Imagenex systems has a major impact on the resulting data density. Plate 2a shows that the faster head speed of the *Jason*/Imagenex system allows it to collect much denser data along track than the *Alvin*/Mesotech system, other parameters being equal. The cross-track data density depends on the altitude, head speed, and range setting of the sonar. The along-track density depends on these factors plus the sector size, the forward speed of the submersible, the consistency of speed and heading, and the amount of overlap between adjacent swaths. Thus, when gridding scanning sonar data, the optimal grid cell size and amount of interpolation between grid cells must be tailored to each survey.

We generally grid the scanning sonar data at either a 2- or 4-m grid cell size with a nearest-neighbor algorithm, and we interpolate out to a radius of 10–40 m from each grid node. The grid cell and interpolation radius sizes used for specific figures are indicated in the captions. The reason for using a relatively small grid cell size is to preserve the high-resolution (across-track) information contained within each sonar sweep. Interpolation between grid cells fills any small gaps (along track) based on data in the nearest sweeps. Picking a larger grid cell size would also help fill in the gaps between sweeps but at the expense of losing the fine-scale information within the sweeps. Our main goal in the gridding process is to display the maximum information content without introducing false features, yielding a quantitative representation of the seafloor for geological interpretation. We use Generic Mapping Tools (GMT) software [*Wessel and Smith*, 1991] to grid and make maps from the scanning sonar data.

3. Results

Between 1993 and 1999, we collected scanning sonar data on 21 *Alvin* and 8 *Jason* dives at eight specific sites along the Juan de Fuca Ridge. The high-resolution bathymetry enables us to investigate the linkages between hydrothermal vents and geologic structures at recent eruption sites. The surveys also show differences in the morphology of recent pillow and sheet flows that can be interpreted in terms of eruption conditions. Most of our surveys were collected on the CoAxial segment (Figure 1), where a dike intrusion and volcanic eruption occurred in 1993 [*Dziak et al.*, 1995; *Embley et al.*, 1995; *Fox et al.*, 1995; *Embley et al.*, 2000]. Additional data are presented from the Cleft segment (Figure 2), which has also experienced recent eruptions [*Normark et al.*, 1986; *Embley and Chadwick*, 1994]. Both segments have a variety of low- and high-temperature hydrothermal vent sites and recent lava flows with differing morphology.

We describe the results from each scanning sonar survey. We include AMS-60 and SeaMARC I side-scan sonar images (collected in 1996 and 1987, respectively) with a comparable resolution of 2–4 m because they present complementary views of the seafloor and independently confirm the features displayed in the scanning sonar maps. Both the AMS-60 and SeaMARC I are deep-towed sonar systems and are typically towed 100–200 m above the seafloor for swath widths of 1–2 km.

3.1. CoAxial Flow Site

At the CoAxial Flow site, where the 1993 eruption occurred, scanning sonar surveys and submersible observations revealed that grabens extend from both the northern and southern ends of the 1993 lava flow [*Chadwick and Embley*, 1998; *Embley et al.*, 2000]. The grabens range in dimension from 10 to 50 m wide and from 5 to 15 m deep. To the north of the main 1993 flow, a series of small, isolated flows of 1993 lava erupted out of the fissure/graben system, which extends at least 1.5 km to the north (Figure 1b). A Mesotech survey just north of the main 1993 flow shows that these satellite flows are either confined within the graben or barely overflow it (Plate 1b and Figure 3). To the south, a

graben extends 700 m from the main 1993 lava flow (Plate 3). Beyond the southern end of this well-defined graben, a narrow zone of cracks, small grabens, and fractured rock extends for another 5 km along the strike of the neovolcanic zone (Figure 1b). A Mesotech survey was conducted ~3.5 km south of the 1993 flow (Plate 4a) where *Alvin* observers mapped a 5-m-wide zone of stained and broken rock that appeared to be brecciated in place and downdropped 1–2 m. This disrupted zone was followed for hundreds of meters along strike and is visible in individual Mesotech profiles (Plate 4b) and in sidescan sonar imagery (Plate 4d). However, the survey coverage was not dense enough for these minor structures to be discernible in the gridded Mesotech bathymetry (Plate 4c).

Chadwick and Embley [1998] interpreted that these grabens and zones of cracking did not exist before the 1993 CoAxial eruption and that they formed directly above the 1993 dike where the dike top was at shallow depth, uprift and downrift from the lava flow. Diffuse hydrothermal venting was active within the small grabens and cracked zones for several months after the 1993 eruption, as the underlying dike rapidly cooled [*Embley et al.*, 2000]. The unburied grabens and zones of cracking thus trace the path of the subsurface dike that fed the 1993 lava flows and may have accommodated much of the near-surface extension during this seafloor spreading event, as is sometimes observed on land [*Rubin*, 1992].

An additional survey at the Flow site was collected over the central part of the 1993 lava flow (Plate 2) using combined data from both the Mesotech and Imagenex sonars (on *Alvin* and *Jason*, respectively). Submersible observations showed that the 1993 CoAxial lava flow was fed from a 2.5-km-long eruptive fissure and produced mainly pillow lavas [*Embley et al.*, 1995, 2000]. However, the scanning sonar bathymetry reveals that the morphology of the flow is characterized by discrete circular mounds, 10–40 m high and 100–300 m in diameter, that are superposed on a linear pillow ridge. This morphology is different from the general hummocky character of many pillow lava flows [*Bryan et al.*, 1994; *Smith et al.*, 1995; *Head et al.*, 1996; *Smith and Cann*, 1999] because in this case the mounds are aligned only along the eruptive fissure. We interpret that this morphology developed because the 1993 CoAxial flow evolved from being fed from a line source during its initial stages to erupting from isolated point sources in later stages. Such localization of output is commonly observed during fissure eruptions on land [*Richter et al.*, 1970; *Swanson et al.*, 1979; *Wolfe et al.*, 1988]. This occurs because the narrower parts of the feeder dike are the first to become blocked as magma solidifies against the dike walls, thereby focusing extrusion to the now isolated and wider parts of the eruptive fissure for the remainder of the eruption [*Delaney and Pollard*, 1982; *Bruce and Huppert*, 1989]. This localization usually takes place within the first several hours to half day of a fissure eruption [*Bruce and Huppert*, 1989]. Thus we conclude that the 1993 CoAxial eruption probably lasted longer than this duration, consistent with estimates based on lava morphology and analog experiments [*Gregg and Fink*, 1995]. The point source character of the morphology of the 1993 lava flow is impossible to discern from visual observations alone, even though one of the longest-lived hydrothermal vent sites visited by submersibles on the 1993 flow was located on the crest of one of these circular mounds (marker 6A in Plate 2b).

Hydrothermal venting on the crest of the 1993 lava flow had nearly stopped by 1995, probably due to its high porosity [*Pruis and Johnson*, 1998] and consistent with similar rapid cooling of other recent pillow mound lavas noted by direct bare rock heat flow measurements [*Johnson and Hutnak*, 1997]. Pillow mounds like the 1993 CoAxial flow are porous and permeable because they form by the accumulation of individual pillows which erupt from the crest and flow down the sides [*Perfit and Chadwick*, 1998]. Pillow lavas erupt at relatively low extrusion rates [*Griffiths and Fink*, 1992; *Gregg and Fink*, 1995] and form crusts before they coalesce with adjacent pillows, thus leaving significant void space between lobes. A low extrusion rate also causes pillows to cool and solidify before they can advance very far from the eruptive vent. Consequently, they pile up to thicknesses of tens of meters; for example, the 1993 CoAxial flow is up to 29 m thick [*Chadwick et al.*, 1995]. Another recent pillow lava flow, located ~700 m to the east of the 1993 flow, reaches 37 m in thickness and is constrained to have erupted between 1982 and 1991 by repeated multibeam surveys [*Chadwick et al.*, 1995]; it has not been surveyed in detail, however (Plate 2). The high-resolution bathymetric surveys at the Flow site help to characterize the eruption that produced the 1993 pillow mound and to document the throughgoing extensional structures that were hydrothermally active following the event.

3.2. CoAxial Floc Site

The Floc site is located along the central part of the CoAxial segment (Figure 1a), ~25 km south of the Flow site. It was also influenced by the 1993 dike intrusion, although no lava was extruded at the site [*Embley et al.*, 1995, 2000]. The Floc site was named because an intense microbial bloom occurred at low-temperature hydrothermal vents immediately after the 1993 intrusion/eruption [*Holden et al.*, 1995; *Juniper et al.*, 1995; *Holden et al.*, 1998]. A composite Mesotech/Imagenex survey at Floc, collected during seven *Alvin* and two *Jason* dives over 3 years, extends for 1.8 km along and 1.4 km across axis (Figure 4a). The bathymetry shows the relationships between seafloor structures, previous eruptive vents, and the new hydrothermal vent sites that were created by the 1993 intrusion (Plate 5).

The diffuse hydrothermal vent sites active after the 1993 intrusion were all located along a preexisting (but

Plate 3. Maps of the graben at the southern end of the 1993 lava flow at the CoAxial Flow site that was hydrothermally active immediately after the eruption (location shown in Figure 1b). The trend of the graben changes slightly where it intersects an older pillow mound. (a) Pattern of soundings from Mesotech sonar on *Alvin* dives 2671 and 2994 used to make map in Plate 3b. (b) Bathymetric map from soundings in Plate 3a (4-m grid cell size; 20-m interpolation radius; 1-m contours). Red outline shows southern end of 1993 lava flow. (c) AMS-60 side-scan sonar image (1-m grid cell size; arrow shows insonification direction; white is high reflectivity, black is acoustic shadow).

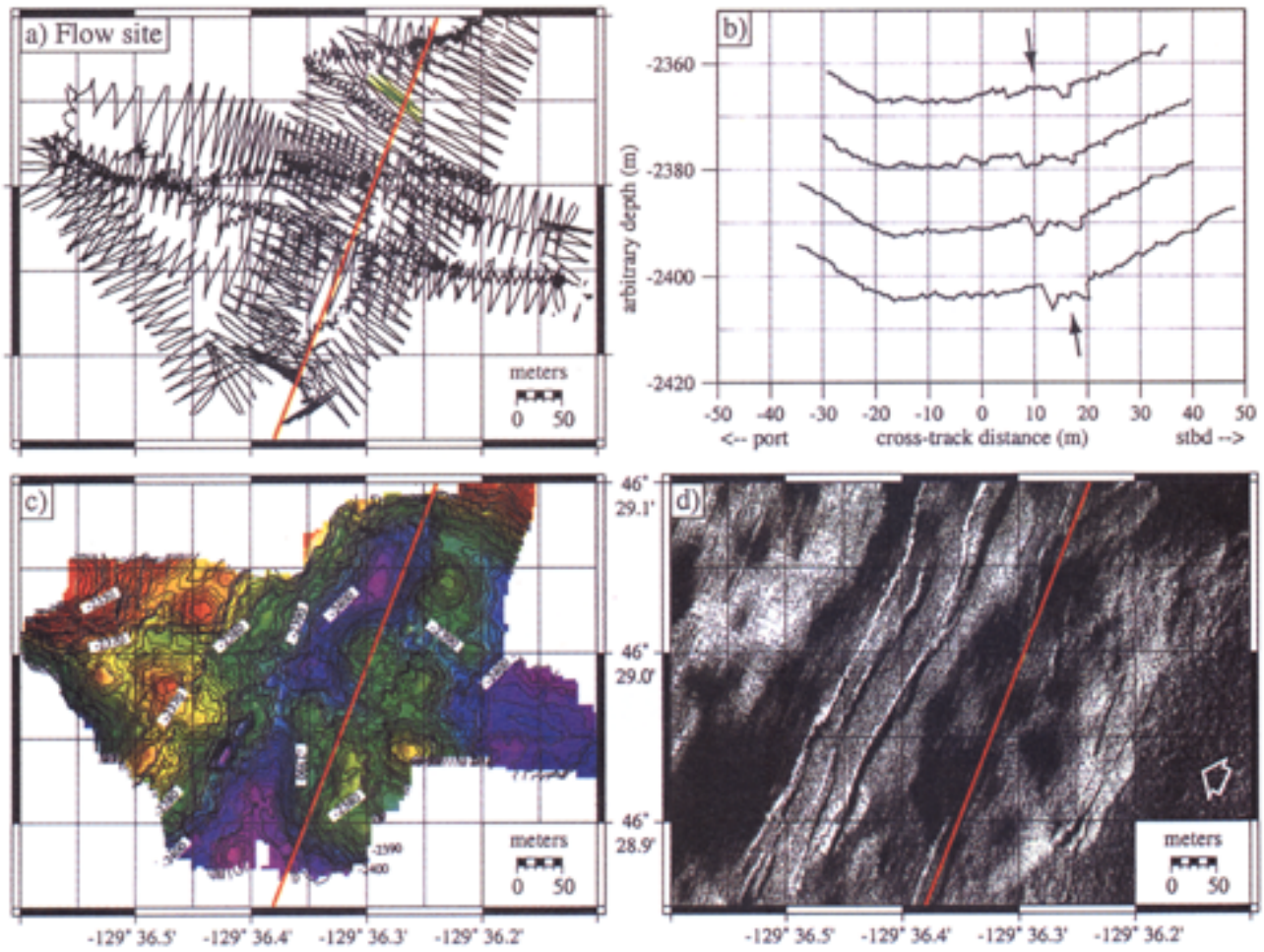

Plate 4. Maps of an area 3.5 km south of the 1993 lava flow at the CoAxial Flow site (location shown in Figure 1b). (a) Mesotech soundings from *Alvin* dives 2990 and 2992; soundings in green are shown as profiles in Plate 4b. (b) Selected depth profiles (green lines in Plate 4a) separated by arbitrary depth for clarity. Arrows show small graben along trend of 1993 intrusion (red line in Plate 4c). (c) Bathymetric map (4-m grid cell size; 40-m interpolation radius; 1-m contours). The red line shows location of fissures and small grabens that were hydrothermally active after the intrusion. Although these structures appear in profiles (Plate 4b), they are not well resolved in the gridded bathymetry because they are small and the sonar coverage is not adequate. (d) AMS-60 side-scan sonar image of the same area (2-m grid cell size; arrow shows insonification direction; white is high reflectivity, black is acoustic shadow), showing minor structures along the 1993 intrusion path (red line). The prominent grabens west of this path are older rift zone structures.

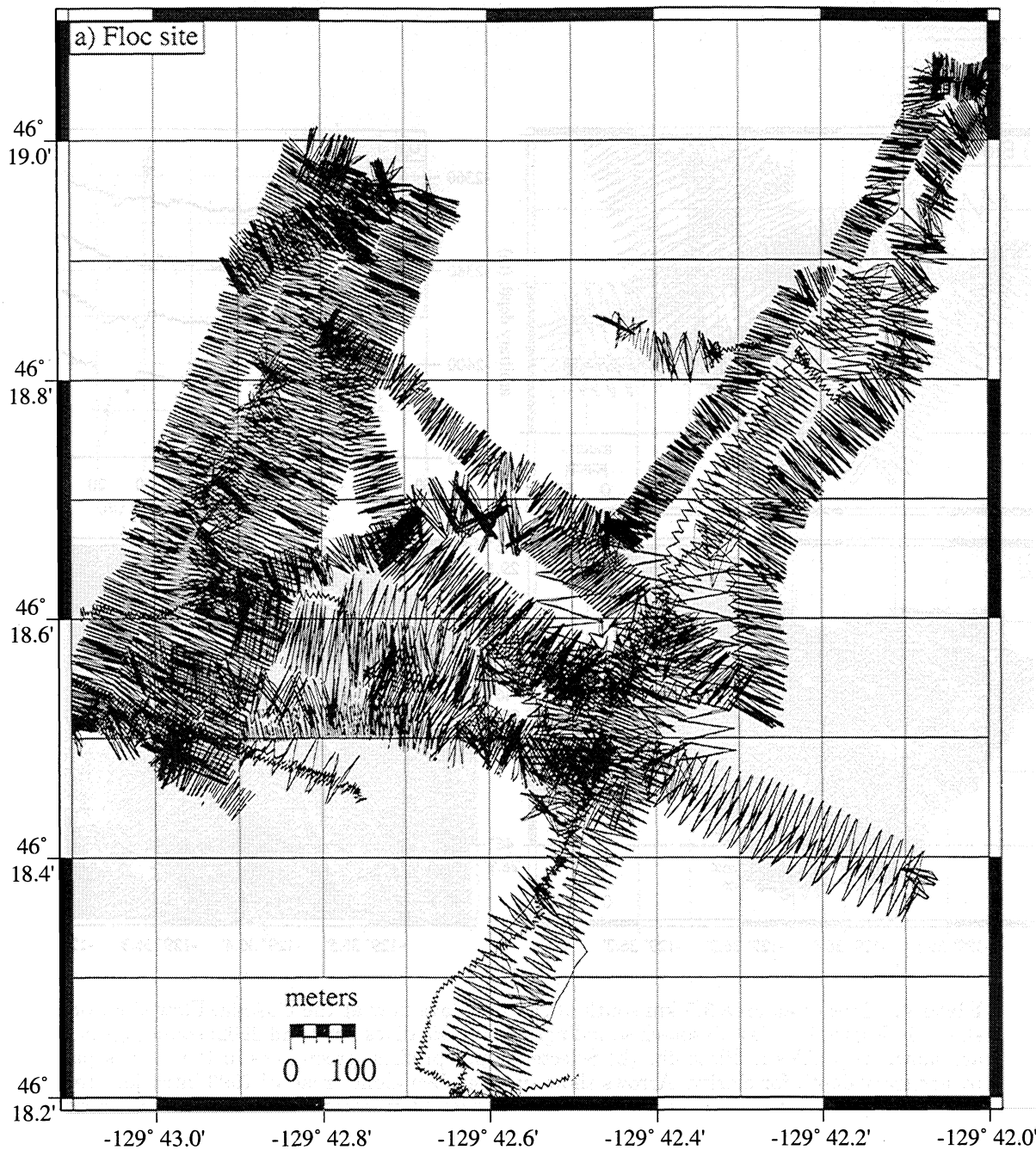

Figure 4. Maps of the CoAxial Floc site (location shown in Figure 1c). (a) Pattern of combined Mesotech and Imagenex sonar soundings from *Alvin* dives 2789, 2791, 2793, 2946, 2947, 2951, and 2995 and *Jason* dives 188 and 189. (b) AMS-60 side-scan sonar mosaic of the same area (4-m grid cell size; dashed line shows sidescan towfish tracks; arrows show insonification direction; white is high reflectivity, black is acoustic shadow). Bathymetry of same area as shown in Plate 5.

possibly reactivated) fissure/graben system on the axis of spreading. The grabens that were hydrothermally active are ~10 m deep and 20 m wide, similar in size to those at the Flow site. The red dots in Plate 5 are markers located along the western edge of this system, which cuts through older pillow mounds (north of huge diffuse vent, "HDV," in Plate 5) and low-lying sheet flows (south of HDV). The fissure/graben system at Floc is interpreted to be pre-existing because a pre-1993 sheet flow south of HDV clearly mantles the structures near marker 2 (M2 in Plate 5) [*Embley et al.*, 2000]. The hydrothermal venting was more or less continuous along strike, but the high-resolution bathymetry shows that where there is more than one parallel fissure, the venting was consistently found on the westernmost structure.

The fissure/graben system that was hydrothermally active is located 700 m east of the most recently erupted lava flows in the area (Figure 1c and Plate 5). These

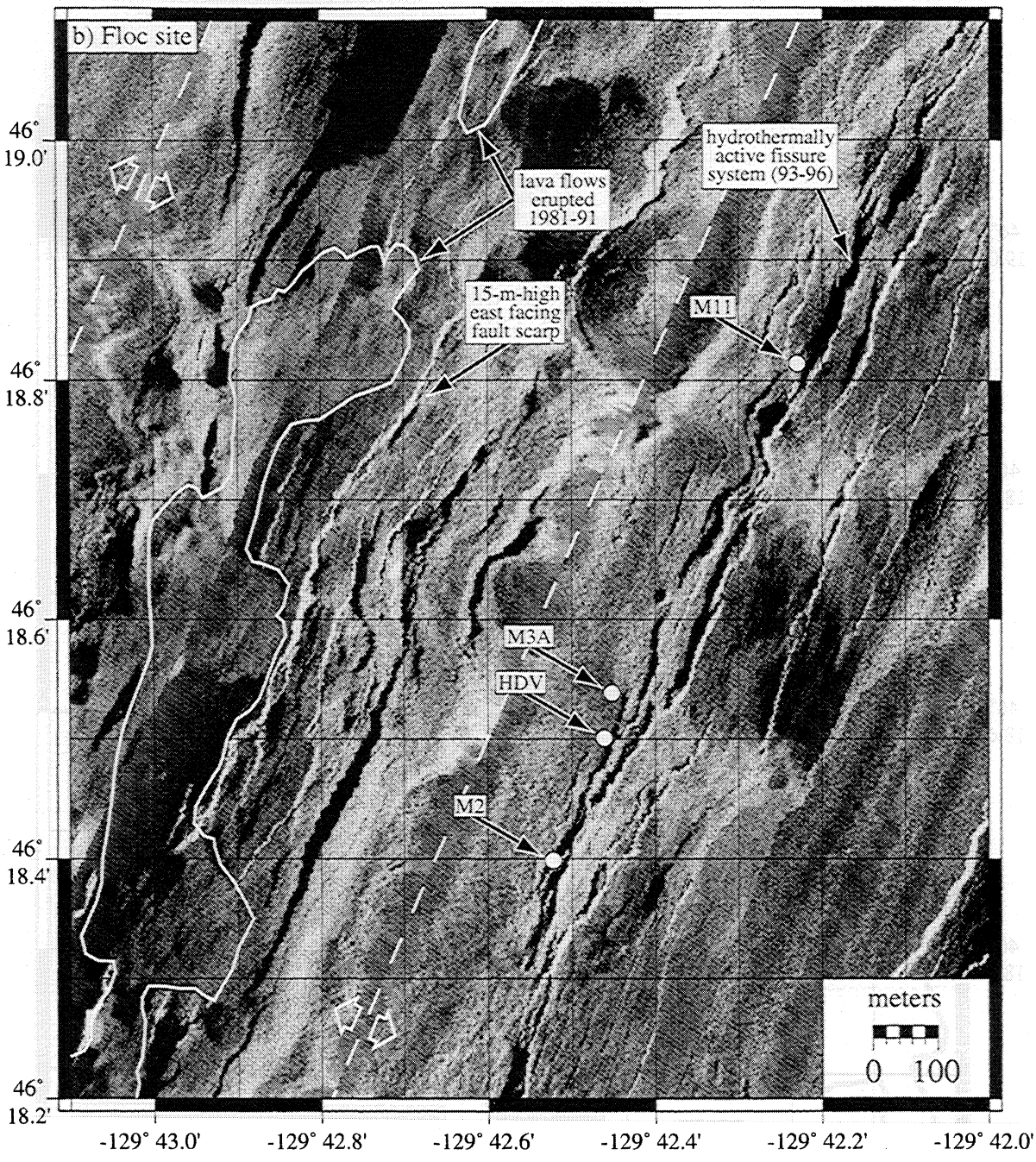

Figure 4. (continued)

older flows are a series of elongate pillow lava mounds that erupted between multibeam bathymetric surveys in 1981 and 1991 and were mapped by camera tows in 1994 [*Embley et al.*, 2000]. The scanning sonar bathymetry shows that these older pillow flows are also characterized by circular accumulations of lava 100–200 m in diameter (Plate 5), suggesting that the latter stage magmatic output was again from point source eruptive centers along the eruptive fissure, similar to the case at the Flow site. Side-scan sonar imagery of the hydrothermally active fissure system (Figure 4b) shows that its shape and character, including bifurcations and en echelon steps, is faithfully depicted in the scanning sonar bathymetry.

Embley et al. [2000] interpreted that the 1993 Co-Axial dike also underlies the Floc site and probably produced an increment of extension across the fissure/graben system when it intruded. The dike provided new heat and increased permeability, which allowed new hydrothermal vent sites to localize there [*Butterfield et al.*, 1997; *Cherkaoui et al.*, 1997] and to bring subseafloor microbes to the surface [*Delaney et al.*, 1998]. These vents were quickly colonized by vent macrofauna within a year after the 1993 intrusion, but since the dike had

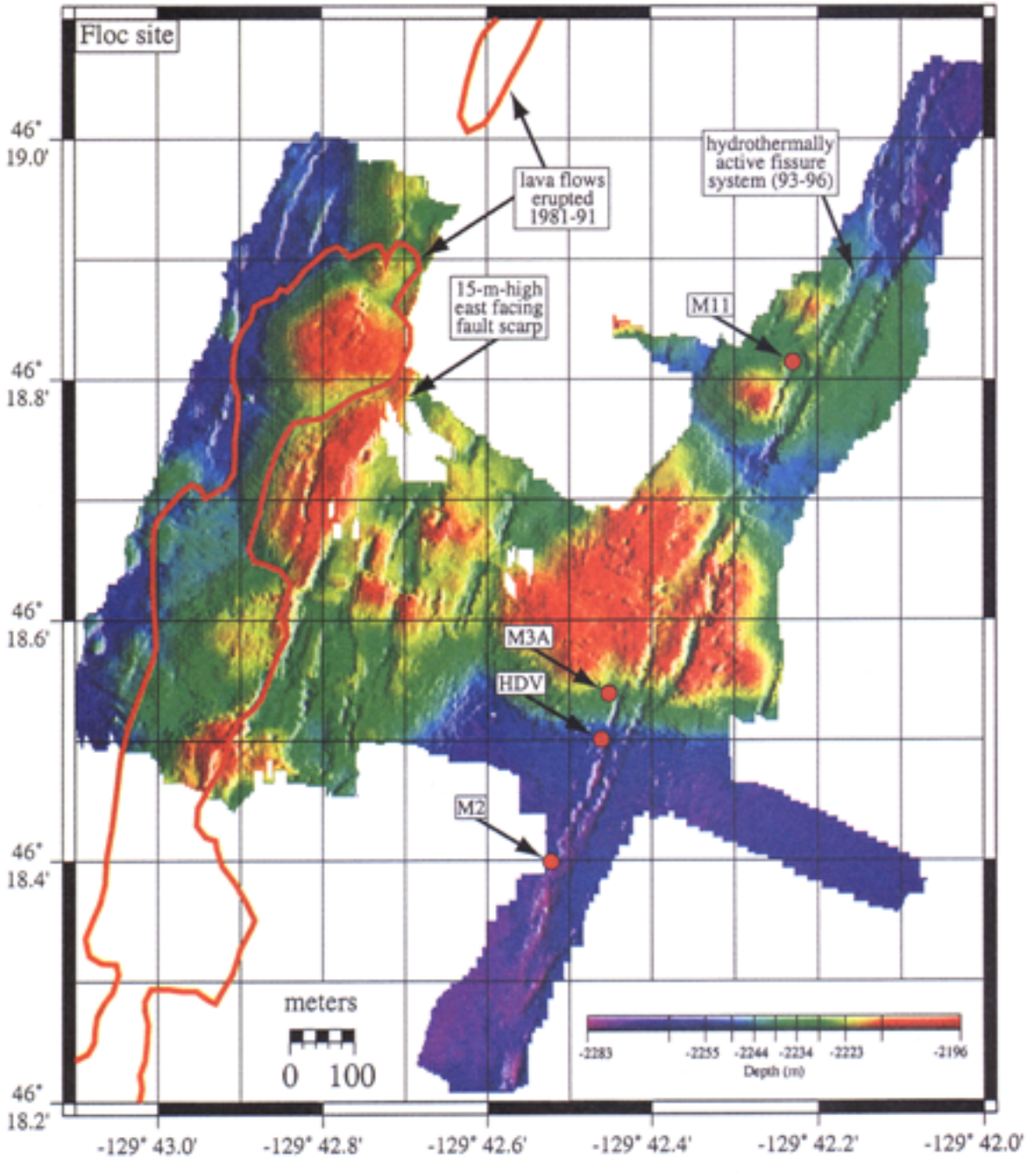

Plate 5. Map of the CoAxial Floc site (location shown in Figure 1c). Bathymetric map (4-m grid cell size; 40-m interpolation radius). Lava flows erupted between 1981 and 1991 (red outline) and marker locations along fissure/graben system that was hydrothermally active immediately following the 1993 dike intrusion (red dots) are shown. Scanning sonar soundings and sidescan mosaic of same area shown in Figure 4.

only a limited reservoir of heat, the vents declined with time and became inactive by 1996 [*Tunnicliffe et al.*, 1997; *Baker et al.*, 1998]. The offset of the 1993 dike trend from the location of earlier eruptions, both at the Floc and Flow sites, shows that the neovolcanic zone (the area within which diking is focused) along the CoAxial segment is ~1 km wide for eruptions spanning a decade [*Embley et al.*, 2000]. The scanning sonar bathymetry at the Floc site again demonstrates that recent pillow flows evolved from line source to point source vents and that the hydrothermal response to the 1993 dike intrusion was tightly focused along individual throughgoing extensional structures.

3.3. CoAxial Source Site

The Source site is located ~20 km south of the Floc site, near the shoalest part of the segment (Figure 1a), and it hosts the only known high-temperature hydrothermal venting along the CoAxial segment [*Embley et al.*, 2000]. The Source site is just south of the latitude where the 1993 earthquake swarm initiated before migrating north to the Flow site [*Dziak et al.*, 1995], but there are no magmatic, chemical, or thermal indications that the Source site was affected by the 1993 intrusion [*Butterfield et al.*, 1997; *Embley et al.*, 2000]. On the basis of Sea Beam bathymetry the vent field at the Source site appears to be located on top of a constructional pillow ridge (Figure 1d). Mesotech sonar bathymetry, however, shows that the vents are located along a 10-m-high, west facing normal fault on the crest of this ridge (Plate 6b). This survey was one of our earliest and has relatively sparse data coverage (Plate 6a), but the fault scarp stands out in individual depth profiles along the vent line (Plate 6c). Submersible observations at the site suggest that the fault is isolated and not part of a graben.

The existence of a normal fault so close to the ridge axis at this spreading rate is unusual [*Perfit and Chadwick*, 1998] and is in contrast to the Floc and Flow sites where mostly fissures and grabens are observed on-axis and normal faults are generally found off-axis. This anomaly may be due to the Source site's setting within the overlap region with the north rift zone of Axial volcano (Figure 1a) and, consequently, may have different tectonic behavior from the rest of the CoAxial segment. In any case, hydrothermal activity at this site is apparently unrelated to the 1993 event [*Embley et al.*, 2000]. The fault at the Source site appears to have established a conduit for vent fluids down to a stable heat source that probably is longer-lived than the ephemeral heat input from the 1993 dike intrusion that caused short-lived hydrothermal venting along the rest of the segment.

3.4. North Cleft Monolith Site

The Cleft segment is the southernmost segment of the Juan de Fuca Ridge (Figure 2a), and the Monolith site is a high-temperature hydrothermal vent system located at the northern end of this segment (Figure 2b). North Cleft is another location where hydrothermal vents are distributed along the trend of recent eruptive fissures or their buried feeder dikes. A series of new pillow lava mounds and a young sheet flow (NPM and YSF, respectively, in Figure 2b) erupted during the early to mid-1980s, probably during separate events [*Chadwick and Embley*, 1994; *Embley and Chadwick*, 1994]. Low-temperature hydrothermal venting that diminished with time was observed following these events along the eruptive axis of both the NPM and the YSF. *Embley and Chadwick* [1994] interpreted this ephemeral low-temperature venting as a consequence of rapid cooling of the eruptive dikes whereas the high-temperature vent sites were rooted in a larger magma body beneath the YSF area. The Monolith site lies just north of the northern tip of the eruptive fissure for the YSF and includes the Monolith and Fountain high-temperature black smoker chimneys (Plate 7). The Monolith chimney is ~20 m north of the end of the YSF, whereas the Fountain chimney is located along the fissure system that links the YSF and NPM eruptive sites [*Embley and Chadwick*, 1994]. Both Monolith and Fountain had their vent fluid chemistry perturbed by the recent eruptions [*Butterfield and Massoth*, 1994], and both sulfide chimneys are interpreted to be older than, although rejuvenated by, the recent eruptions [*Koski and Jonasson*, 1994].

We conducted a Mesotech survey at the Monolith site to examine the relationship between venting and volcanic structures at the site (Plate 7a). The high-resolution bathymetry shows that both the Monolith and Fountain high-temperature vent sites are located along the eastern edge of a 25-m high ridge. On the basis of the Mesotech survey (Plate 7b), side-scan sonar imagery (Plate 7c), and observations from *Alvin*, this ridge is interpreted to be a large "lava rise" because it has a characteristic morphology of a flat top that is separated from steeply inclined sides by prominent cracks or "lava inflation clefts" [*Walker*, 1991]. Lava rises (or "pressure plateaus") are formed by the prolonged injection of molten lava under its own thick surface crust which uniformly raises the central portion of the affected flow while steeply tilting the edges. Lava inflation clefts form as hinge zones between the flat top and tilted sides of the lava rise when the sides progressively rotate during uplift. These morphologic features have been documented in basaltic lava flows on land emplaced on relatively gentle slopes under specific eruptive conditions [*Wentworth and Macdonald*, 1953; *King*, 1982; *Guest et al.*, 1984; *Walker*, 1991; *Chitwood*, 1994; *Hon et al.*, 1994; *Rossi and Gudmundsson*, 1996]. Although evidence for lava flow inflation has only been recently recognized in the mid-ocean ridge environment [*Applegate and Embley*, 1992; *Bryan et al.*, 1994], it may actually be more common than on land because of the

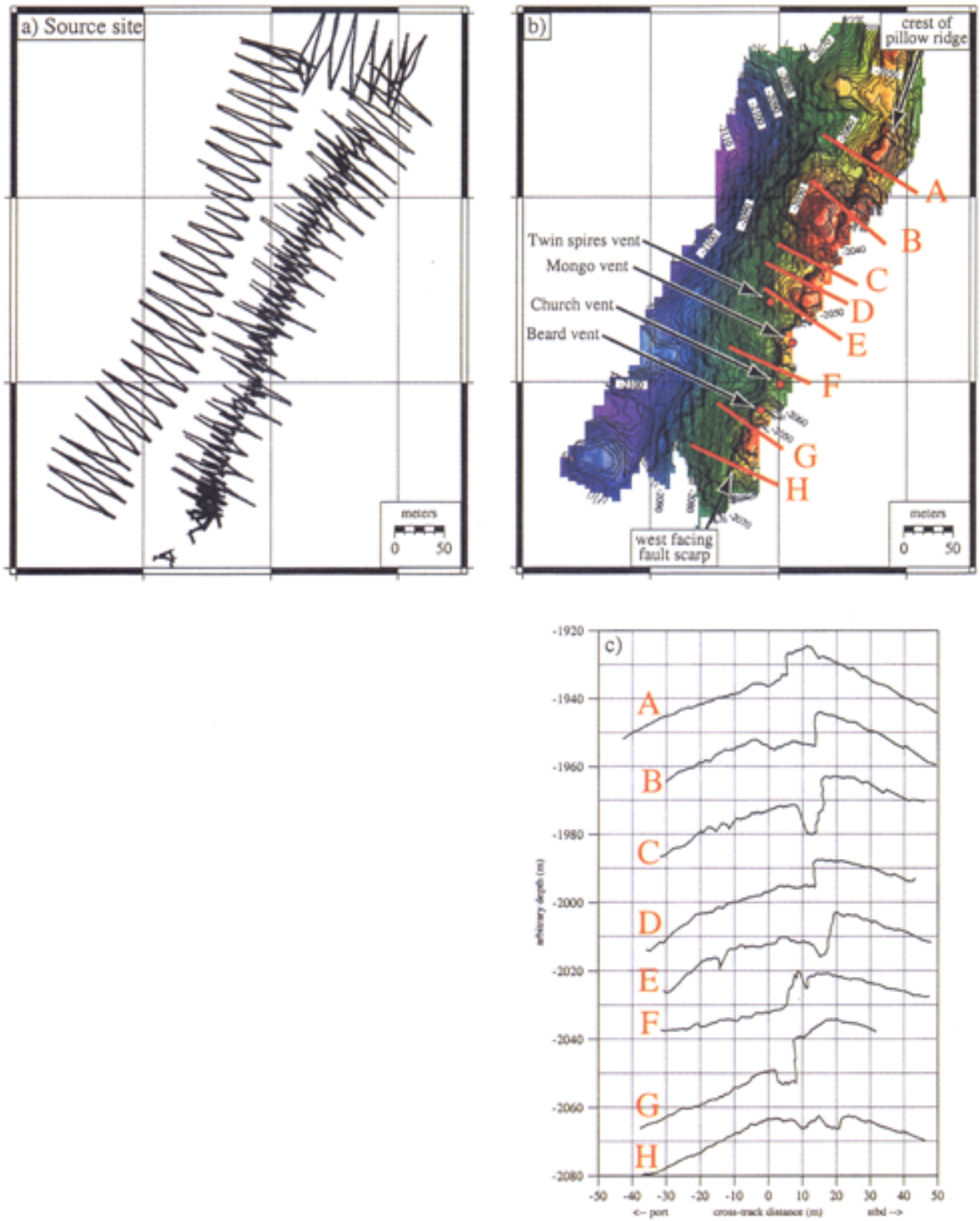

Plate 6. Maps of the CoAxial Source site (location shown in Figure 1d). (a) Pattern of Mesotech sonar soundings from *Alvin* dives 2790 and 2945. (b) Bathymetric map (4-m grid cell size; 40-m interpolation radius; 1-m contours) showing locations of high-temperature vents (red circles) in relation to west facing fault near the crest of a constructional pillow ridge. Lines labeled A–H are locations of individual depth profiles show in Plate 6c. (c) Individual depth profiles (locations shown in Plate 6b) offset from one another by an arbitrary depth for clarity. High-temperature vents are aligned along the west facing fault scarp.

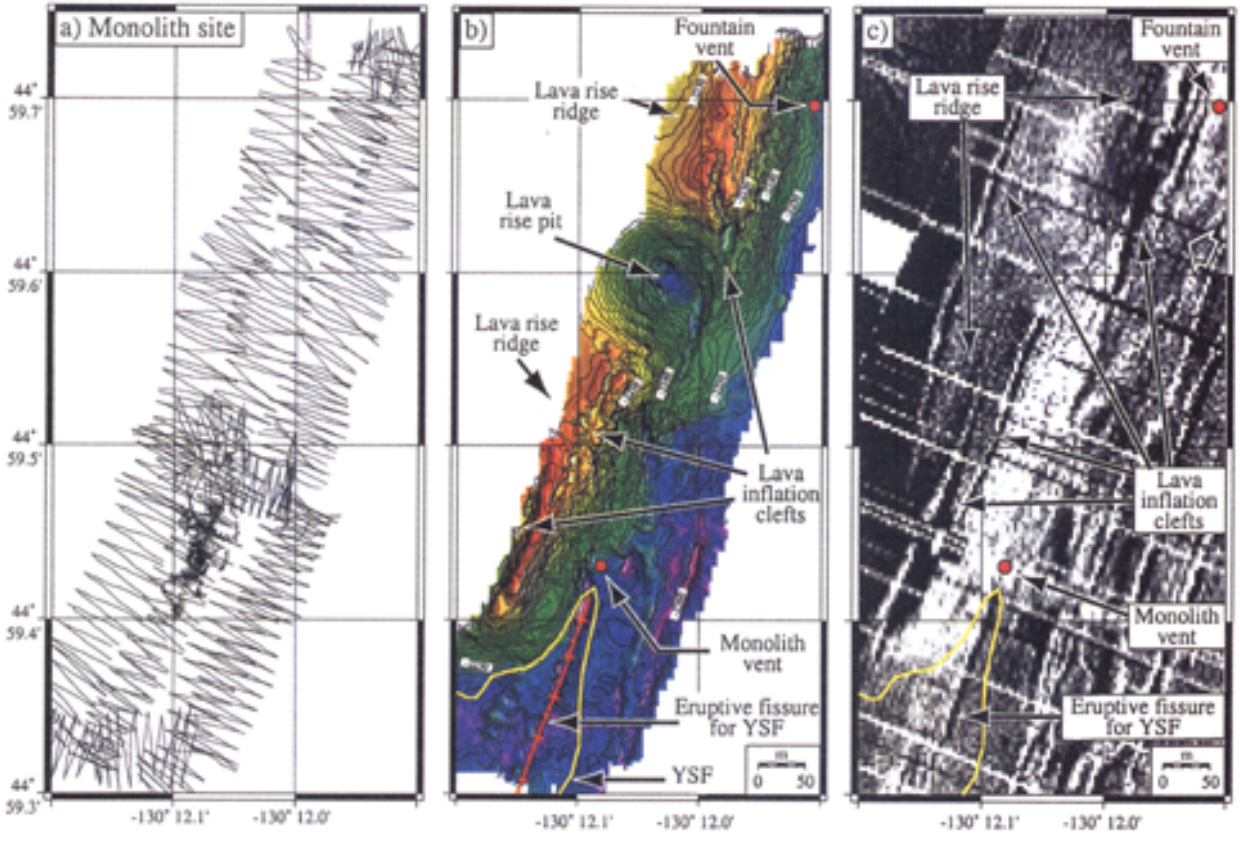

Plate 7. Maps of north Cleft Monolith site (location shown in Figure 2b). (a) Pattern of Mesotech sonar soundings from *Alvin* dives 2811, 2812, and 2944. (b) Bathymetric map (4-m grid cell size; 30-m interpolation radius; 1-m contours) showing locations of Monolith and Fountain high-temperature vents (red circles) in relation to the northern end of the YSF (yellow outline), its eruptive fissure (red hatched line), and the lava rises to the west of the vents (see text for discussion). (c) SeaMARC I side-scan sonar mosaic shows the same structures that were mapped with the Mesotech sonar (4-m grid cell size; arrow shows insonification direction; white is high reflectivity, black is acoustic shadow; light and dark bands trending NW-SE are data dropouts).

more rapid rate of crust growth on submarine lava flows [*Gregg and Fornari*, 1998].

The inflation of submarine sheet flows does not always lead to the formation of lava rises. Submarine lobate sheet flows with lava pillars and collapsed interiors (such as at south Cleft, described below) have also been interpreted to form by lava flow inflation [*Gregg and Chadwick*, 1996; *Chadwick et al.*, 1999]. They do not form lava rises because the erupted volume is relatively small, the effusion rate is relatively high, and the eruption duration is brief (hours), all conditions favoring lava drainback in the waning stages of the eruption [*Perfit and Chadwick*, 1998]. We speculate that lava rises, on the other hand, probably form where lava is erupted at relatively steady eruption rates and over an extended period of time (days-weeks), allowing the construction of larger features that inflate and then solidify in place on the seafloor. More detailed study of these kinds of features on the seafloor is required to test this hypothesis. Examples of lava rises on land are generally between 1 and 20 m thick [*Walker*, 1991; *Chitwood*, 1994; *Rossi and Gudmundsson*, 1996] and therefore the 25-m height of the lava rise ridge at the Monolith site is comparatively large, perhaps indicating a relatively long eruption duration.

The large crack that splits the southern end of the lava rise west of Monolith is 10 m wide and 20 m deep, large enough that *Alvin* could drive inside it during dive 2258 (Plates 7b and 7c). The internal walls of the crack were observed to be thick, massive lavas with columnar jointing, and we interpret that this crack probably formed in the same inflation process that forms tumuli on land [*Walker*, 1991]. The circular reentrant in the ridge between the Monolith and Fountain vents (Plate 7b) is interpreted as a "lava rise pit," formed because the surrounding lava was uplifted rather than due to subsidence of the pit itself [*Walker*, 1991]. This pit is not obvious in the sidescan imagery due to the insonification direction (Plate 7c). Although the hydrothermal vents are found adjacent to the lava rise ridge, we interpret that their location is primarily controlled by the throughgoing fissure system that fed the most recent eruptions rather than being related to the formation of the adjacent older lava rise.

3.5. South Cleft Site

The southern end of the Cleft segment (Figure 2c) is characterized by a distinct "cleft" (from which the segment gets its name) that cuts through a young and otherwise unfissured lobate sheet flow that covers most of the 1-km-wide axial valley floor [*Kappel and Normark*, 1987]. The cleft is a graben-like structure that is 50–100 m wide, 5–30 m deep, and >10 km long. It is interpreted to have been the eruptive vent for the recent lobate sheet flow [*Normark et al.*, 1986]. Three main high-temperature hydrothermal vent areas, Plume, Vent1, and Vent3, are located within the cleft [*Normark et al.*, 1983, 1987].

Previous studies have shown that lobate flows are emplaced as a broad flat sheet with a molten flow interior between upper and lower crusts [*Ballard et al.*, 1979; *Chadwick et al.*, 1999]. In contrast, pillow lava mounds are composed of hummocky piles of individual pillows that do not flow far before they crust over and cool as separate units [*Moore*, 1975; *Perfit and Chadwick*, 1998]. This difference is thought to reflect that sheet flows are fed at higher effusion rates than pillow flows [*Griffiths and Fink*, 1992; *Gregg and Fink*, 1995]. Lobate sheet flows initially spread outward from the eruptive fissure as thin (20–30 cm) flows and then increase in thickness (up to 5 m or more) by lava flow inflation after the margins of the flow stop spreading [*Hon et al.*, 1994; *Gregg and Chadwick*, 1996]. As soon as the effusion rate at the vent declines, flow inflation ends and lava drainback or drainout begins. In this phase, lava in the still molten flow interior drains away either back into, or away from, the vent. This creates extensive areas of collapse where the upper crust founders and hollow cavernous areas where the upper crust remains intact and is supported by pillars or walls. The thickness of the remnant upper crust is usually only a few centimeters, indicating that this sequence of events takes place in only a matter of hours on the basis of predicted rates of crust growth [*Gregg and Chadwick*, 1996; *Gregg and Fornari*, 1998].

We used the Imagenex sonar on *Jason* to collect high-resolution bathymetry at south Cleft. This survey is the largest and most recent and has the densest data coverage of those presented in this paper (Plate 8). The survey is 400 m wide along most of its 4 km length but also includes a 1.6-km-wide cross-axis portion that extends part-way up the axial valley walls (Plate 8a). The survey was made primarily to select sites for seafloor monitoring instruments in the area (W.W. Chadwick et al., A deep-sea observatory experiment using acoustic extensometers: Precise horizontal distance measurements across a mid-ocean ridge, submitted to *IEEE Journal of Oceanic Engineering*, 2001), but it also provides the opportunity to study the morphology of the cleft, the young lava flow, and the physical setting of the Plume and Vent1 hydrothermal vent sites.

The new bathymetry shows that the south Cleft sheet flow has very low relief, most of it due to collapse (Plate 8 and Figure 5). The depth along the rim of the cleft is consistently 2210 m in the southern half of

Plate 8. South Cleft Imagenex survey from *Jason* dives 236 and 265–268 (location shown in Figure 2c). (a) Bathymetric map of Vent1 hydrothermal vent area (2-m grid cell size; 30-m interpolation radius). Location of cross section in Figure 5 shown by X–X'. (b) Bathymetric map of Plume vent area, just south of Plate 8a (2-m grid cell size; 40-m interpolation radius). Distribution of soundings shown in inset maps. Color scale is same on both maps. Dendritic and slot-like drainback patterns shown by "D" and "S" labels, respectively (see text for discussion).

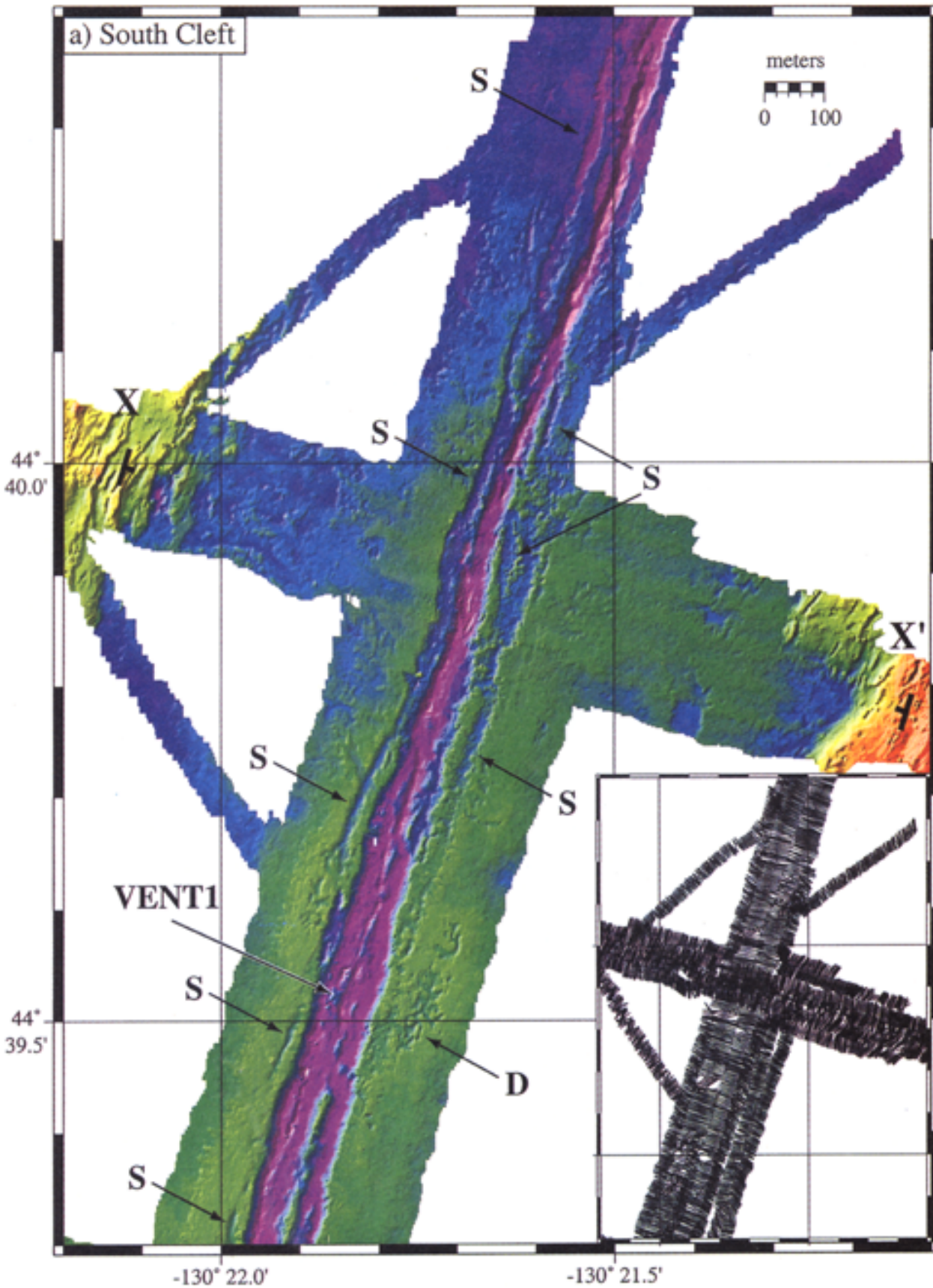
a) South Cleft
meters
0 100
S
X
X'
S
S
S
S
S
VENT1
S
D
S
44° 40.0'
44° 39.5'
-130° 22.0'
-130° 21.5'

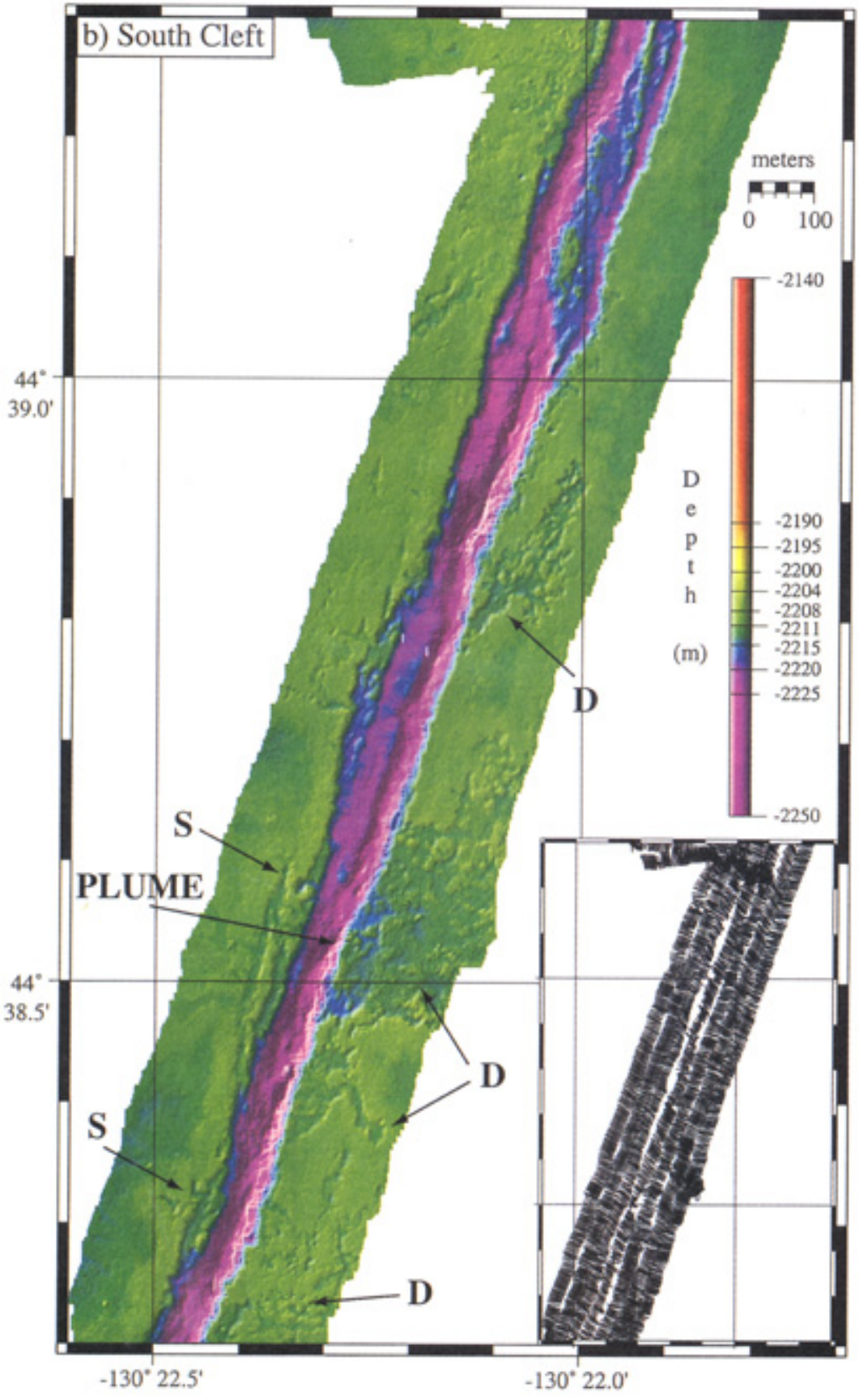
b) South Cleft
meters
0
100
-2140
Depth
(m)
-2190
-2195
-2200
-2204
-2208
-2211
-2215
-2220
-2225
-2250
44°
39.0'
44°
38.5'
-130° 22.5'
-130° 22.0'
S
PLUME
S
D
D
D
D

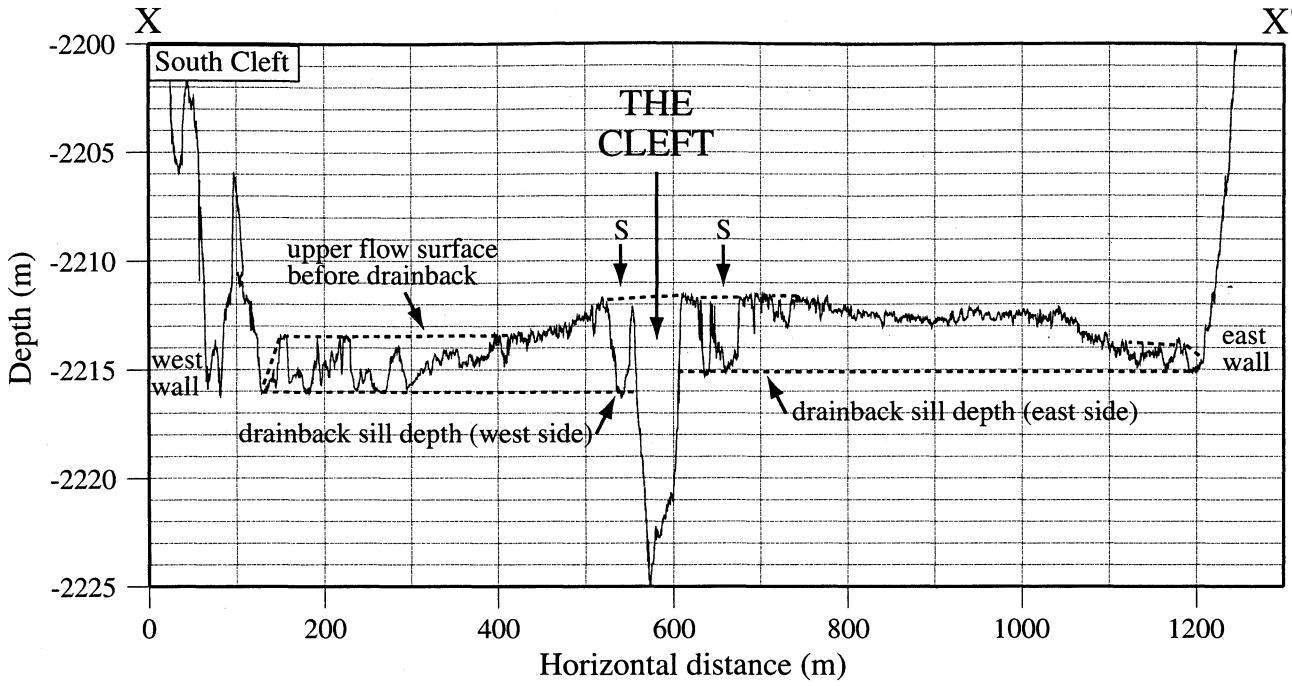

Figure 5. Depth cross section X–X' across south Cleft axial valley (location shown in Plate 8a; 25 × vertical exaggeration) derived from *Jason* depth plus altitude data showing features related to lava drainback into the cleft. Slot-like drainback features shown by "S" labels (see text for discussion).

the survey, and it gradually increases to 2220 m at the north end. The floor of the cleft deepens in the opposite sense, from 2225 m at the northern end of the survey to 2240 m at the southern end. Previous studies had hypothesized that the Plume and Vent1 hydrothermal sites were "centers of eruption" along the cleft [*Normark et al.*, 1986; *Holcomb et al.*, 1987; *Normark et al.*, 1987], but there is no evidence for this in the scanning sonar bathymetry. For example, the cleft is not especially wide at Plume and Vent1, nor is there any indication that the eruption was focused or lasted longer at these sites. Instead, the bathymetry suggests that the eruption was relatively uniform in output and duration along its entire length. This is in contrast to the evidence for an evolution from line-source to point source output during pillow mound eruptions discussed earlier. There is a broad area of collapse on the east side of the cleft at the Plume site (Plate 8b), but this probably is more related to the drainback phase of the eruption than the effusion phase. Drainback may have been concentrated in this area simply because it was a relatively low spot on the rim of the cleft.

A profile across the axial valley (Figure 5) shows that the seafloor deepens by a few meters between the rim of the cleft and the base of the valley walls, consistent with the cleft having been the source of lavas that flooded the entire floor. The cross section also shows that collapse areas due to lava drainback are 1–4 m deep and are generally deepest near the cleft where there is also a concentration of lava pillars. The bottom of the cleft tapers to a narrow fissure in many parts of the survey (Plate 8 and Figure 5). The maximum thickness of the flow before drainback was apparently at least 5 m. The maximum depth or "base level" of the collapses is consistent on each side of the cleft (Figure 5), suggesting that the entire width of the flow (even parts near the valley walls) drained back into the cleft at the end of the last eruption. This makes sense because the axial valley limited the outward advance of the lava, and as soon as the eruption stopped, the deep cleft was the natural place for lava to drainback into. Interestingly, this base level is 1 m deeper on the west side of the cleft than on the east, apparently due to local variation in the "sill depth" along the rim of the cleft (Figure 5).

There are two common but very different patterns of drainback evident in the south Cleft bathymetry. One pattern of collapse is somewhat dendritic, with channels that lead back into the cleft (labeled D in Plate 8). The other common pattern consists of long, narrow, slot-like collapse depressions (labeled S in Plate 8 and Figure 5) oriented subparallel to the cleft but separated from it by intact lava. These slot-like features are 5–20 m wide and 100–400 m long and are located within ~50 m of the edge of the cleft. Some of the slot-like depressions have one end that merges with the cleft and submersible observations confirm that these were major sites of lava drainback. Other slot-like collapses do not appear to merge with the cleft but could be connected in the subsurface. The fact that these long, narrow troughs are subparallel to the cleft is curious because one might

expect drainback to occur directly toward (normal to) the cleft. The cleft-parallel orientation of these features suggests that they form behind physical obstructions to drainback along the rim of the cleft. For example, in the cross section of Figure 5, there are walls on both sides of the cleft that would prevent lava from draining directly into the cleft. Instead, lava flowing back toward the cleft at this location would have to be diverted either north or southward around these walls before it could drain into the cleft (Plate 8a). Submersible observations suggest these walls are made of coalesced lava pillars that formed on the rim of the cleft, some possibly during previous eruptions. The walls or islands within the cleft between the Vent1 and Plume sites (Plate 8) may have formed in a similar way. They are capped by intact lobate lava, indicating that the flow completely filled the cleft to this level during the eruption.

A comparison of the scanning sonar bathymetry with previously collected SeaMARC I side-scan sonar data [*Embley and Chadwick*, 1994] shows that these slot and dendritic drainback features are visible but subtle in the side-scan imagery. The slot features could be mistaken for fault scarps without the bathymetry. Also, areas of very flat lineated lava [*Chadwick et al.*, 1999] in the floors of some collapse areas create distinct patches of low backscatter in the side-scan imagery. *Kappel and Normark* [1987] mistakenly interpreted some of these low backscatter patches as islands of older heavily sedimented lava surrounded by younger flows (kipukas). However, these new data show that the variation in backscatter on the young lobate flow at south Cleft is due to morphological variation within the flow rather than age differences between flows.

We interpret that the pattern of drainback features in the young lobate flow at south Cleft was controlled by local variations in the sill depth along each side of the cleft. This interpretation emphasizes the view that the cleft is a persistent eruptive center and is not a static feature. Each new lava flow is influenced by the microtopography that exists at the time it erupts, but it also overprints the preexisting structure. In this way, the cleft is similar to the axial summit trough described on the northern East Pacific Rise [*Fornari et al.*, 1998]. At south Cleft the dominance of drainback and the lack of well-developed channels leading off axis, as has been observed on the southern East Pacific Rise [*Ryan et al.*, 1999], is due to the laterally restrictive physical setting within an axial valley.

The new bathymetry shows that the morphology of the south Cleft sheet flow is in marked contrast to the pillow mounds on the CoAxial segment and the lava rise ridge at north Cleft. The north and south Cleft sites are similar in that the most recent eruptions have issued from prominent fissure systems that clearly mark the current axis of spreading and are also the current locus of high-temperature hydrothermal venting. The main difference between lobate sheet flows and lava rises is that lobate sheet flows inflate and drainout over a very short period of time, whereas lava rises apparently grow at a slower rate as evidenced by the large cracks in their thick upper crust, the lack of drainout features, and their larger range of thicknesses.

4. Conclusions

High-frequency scanning sonar systems mounted on submersibles produce high-resolution depth profiles that can be gridded at a resolution of 2 to 4 m. Bathymetric maps made from these grids can be contoured at 1-m intervals and greatly aid in the interpretation of geological features on the seafloor. These maps are at a scale much larger than can be appreciated by near-bottom visual surveys and they have a resolution nearly 2 orders of magnitude finer than provided by near-surface systems. These seafloor maps place bottom observations and samples into a broader and more meaningful spatial context. The faster head speed of the Imagenex sonar makes it better suited to this purpose than the Mesotech sonar because the Imagenex can collect much denser data in the along-track direction than the Mesotech under the same survey conditions.

Our high-resolution bathymetric surveys on the CoAxial and Cleft segments of the Juan de Fuca Ridge show that hydrothermal vents are consistently located along recent eruptive fissures, narrow zones of extension above buried dikes, or faults within the neovolcanic zone. The structures that host low- and high-temperature hydrothermal vents are not fundamentally different in morphology; they all form by faulting and fissuring over dike intrusions during seafloor spreading events. The persistent high-temperature sites differ from the ephemeral low-temperature ones only in that the structures they are located on apparently tap deeper and longer-lived heat sources.

High-resolution bathymetry can also be used to interpret the style and evolution of seafloor eruptions from the morphology of the lava flows they produce. Scanning sonar data provide the resolution necessary to identify and quantify volcanological features related to lava flow inflation and drainback within sheet flows and lava rises. The superposition of individual circular constructs along the length of recently erupted pillow lava flows on the CoAxial segment implies an evolution from a linear fissure vent to point source vents during pillow-forming eruptions. Previous studies suggest that the recent pillow mounds at north Cleft and the northern Gorda Ridge may also share this morphology [*Chadwick and Embley*, 1994; *Chadwick et al.*, 1998]. In contrast, the lobate sheet flow at south Cleft lacks any such evidence for localization of output along its eruptive fissure, probably because of a higher effusion rate and shorter eruption duration. Similarly, the recent lobate sheet flows at north Cleft and Axial Volcano show no evidence of localization [*Embley and Chadwick*, 1994; *Embley et al.*, 1999]. Since the transition from curtain of fire to isolated vents along eruptive fissures on land

typically takes place between 2 and 12 hours after the eruption onset [*Bruce and Huppert*, 1989], we infer that the duration of lobate sheet flow eruptions is usually less than this range and that the duration of pillow eruptions is correspondingly longer.

Acknowledgments. The data presented in this paper were collected with the submersibles *Alvin* and *Jason*, both operated by the Woods Hole Oceanographic Institution. Many thanks to the submersible pilots who skillfully conducted these surveys despite the lack of scenery when driving for extended periods out of the sight of the bottom. Also thanks to the many scientific observers who helped to collect scanning sonar data during parts of their *Alvin* dives, including Gary Massoth, Jim Holden, John Delaney, Kevin Roe, Verena Tunnicliffe, Dawn Wright, Mike Perfit, Mark Holmes, Byron Ruppel, Maurice Tivey, Mike Hutnak, John Lupton, Hank Chezar, Ian Jonasson, Meg Tivey, and Dave Kadko. Special thanks to Maurice Tivey, who first alerted us to the great potential of scanning sonar bathymetry. Darcy Van Patten helped collect and assemble the *Jason* Imagenex data from CoAxial. Helpful reviews by Joe Cann, Margo Edwards, and Maurice Tivey greatly improved the manuscript. This work was supported by the NOAA/Vents and NSF/RIDGE Programs. PMEL contribution 2225.

References

Agnew, D., NLOADF: A program for computing ocean-tide loading, *J. Geophys. Res., 102,* 5109–5110, 1997.

Appelgate, B., and R. W. Embley, Submarine tumuli and inflated tube-fed lava flows on Axial Volcano, Juan de Fuca Ridge, *Bull. Volcanol., 54,* 447–458, 1992.

Baker, E. T., G. J. Massoth, R. A. Feely, G. A. Cannon, and R. E. Thomson, The rise and fall of the CoAxial hydrothermal site, 1993–1996, *J. Geophys. Res., 103,* 9791–9806, 1998.

Ballard, R. D., R. T. Holcomb, and T. H. van Andel, The Galapagos Rift at 86°W, 3, Sheet flows, collapse pits, and lava lakes of the rift valley, *J. Geophys. Res., 84,* 5407–5422, 1979.

Bradley, A. M., D. R. Yoerger, M. H. Cormier, W. B. F. Ryan, and B. B. Walden, High resolution mapping of a fast spreading mid-ocean ridge with the Autonomous Benthic Explorer, *Eos Trans. AGU, 80*(46), Fall Meet. Suppl., F1072, 1999.

Bruce, P. M., and H. E. Huppert, Thermal control of basaltic fissure eruptions, *Nature, 342,* 665–667, 1989.

Bryan, W. B., S. E. Humphris, G. Thompson, and J. F. Casey, Comparative volcanology of small axial eruptive centers in the MARK area, *J. Geophys. Res., 99,* 2973–2984, 1994.

Butterfield, D. A., and G. J. Massoth, Geochemistry of north Cleft segment vent fluids: Temporal changes in chlorinity and their possible relation to recent volcanism, *J. Geophys. Res., 99,* 4951–4969, 1994.

Butterfield, D. A., I. R. Jonasson, G. J. Massoth, R. A. Feely, K. K. Roe, R. W. Embley, J. F. Holden, R. E. McDuff, M. D. Lilley, and J. D. Delaney, Seafloor eruptions and evolution of hydrothermal fluid chemistry, *Philos. Trans. R. Soc. London, Ser. A, 355,* 369–386, 1997.

Chadwick, W. W. Jr., and R. W. Embley, Lava flows from a mid-1980s submarine eruption on the Cleft Segment, Juan de Fuca Ridge, *J. Geophys. Res., 99,* 4761–4776, 1994.

Chadwick, W. W. Jr., and R. W. Embley, Graben formation associated with recent dike intrusions and volcanic eruptions on the mid-ocean ridge, *J. Geophys. Res., 103,* 9807–9825, 1998.

Chadwick, W. W. Jr., R. W. Embley, and C. G. Fox, SeaBeam depth changes associated with recent lava flows, CoAxial segment, Juan de Fuca Ridge: Evidence for multiple eruptions between 1981–1993, *Geophys. Res. Lett., 22,* 167–170, 1995.

Chadwick, W. W. Jr., R. W. Embley, and T. M. Shank, The 1996 Gorda Ridge eruption: Geologic mapping, sidescan sonar, and SeaBeam comparison results, *Deep Sea Res., Part II, 45,* 2547–2570, 1998.

Chadwick, W. W. Jr., T. K. P. Gregg, and R. W. Embley, Submarine lineated sheet flows: A unique lava morphology formed on subsiding lava ponds, *Bull. Volcanol., 61,* 194–206, 1999.

Cherkaoui, A. S. M., W. S. D. Wilcock, and E. T. Baker, Thermal fluxes associated with the 1993 diking event on the CoAxial segment, Juan de Fuca Ridge: A model for the convective cooling of a dike, *J. Geophys. Res., 102,* 24,887–24,902, 1997.

Chitwood, L. A., Inflated basaltic lava—Examples of processes and landforms from central and southeast Oregon, *Oreg. Geol., 56,* 11–21, 1994.

Cormier, M. H., W. B. F. Ryan, W. Jin, A. Shah, A. M. Bradley, D. R. Yoerger, H. Singh, J. Sinton, R. Batiza, and K. Rubin, Building of the extrusive crust of the EPR at 17°28′S through fissure-fed inflationary lava flows, *Eos Trans. AGU, 80*(46), Fall Meet. Suppl., F1097, 1999.

Delaney, J. R., D. S. Kelley, M. D. Lilley, D. A. Butterfield, J. A. Baross, W. S. D. Wilcock, R. W. Embley, and M. Summit, The quantum event of oceanic crustal accretion: Impacts of diking at mid-ocean ridges, *Science, 281,* 222–230, 1998.

Delaney, J. R., D. S. Kelley, E. A. Mathez, D. R. Yoerger, J. Baross, M. O. Schrenk, M. K. Tivey, J. Kaye, and V. Robigou, Edifice Rex sulfide recovery project: Analysis of submarine hydrothermal, microbial habitat, *Eos Trans. AGU, 82*(67), 72–73, 2001.

Delaney, P. T., and D. D. Pollard, Solidification of basaltic magma during flow in a dike, *Am. J. Sci., 282,* 856–885, 1982.

Dziak, R. P., C. G. Fox, and A. E. Schreiner, The June–July 1993 seismo-acoustic event at CoAxial segment, Juan de Fuca Ridge: Evidence for a lateral dike injection, *Geophys. Res. Lett., 22,* 135–138, 1995.

Embley, R. W., and W. W. Chadwick Jr., Volcanic and hydrothermal processes associated with a recent phase of seafloor spreading at the northern Cleft segment: Juan de Fuca Ridge, *J. Geophys. Res., 99,* 4741–4760, 1994.

Embley, R. W., W. W. Chadwick, Jr., I. R. Jonasson, D. A. Butterfield, and E. T. Baker, Initial results of the rapid response to the 1993 CoAxial event: Relationships between hydrothermal and volcanic processes, *Geophys. Res. Lett., 22.* 143–146, 1995.

Embley, R. W., W. W. Chadwick, Jr., D. Clague, and D. Stakes, The 1998 eruption of Axial Volcano: Multibeam anomalies and seafloor observations, *Geophys. Res. Lett., 26,* 3425–2428, 1999.

Embley, R. W., W. W. Chadwick, Jr., M. R. Perfit, M. C. Smith, and J. R. Delaney, Recent eruptions on the Co-Axial segment of the Juan de Fuca Ridge: Implications for mid-ocean ridge accretion processes, *J. Geophys. Res., 105,* 16,501–16,525, 2000.

Fornari, D. J., R. M. Haymon, M. R. Perfit, T. K. P. Gregg, and M. H. Edwards, Axial summit trough of the East Pacific Rise 9°N to 10°N: Geological characteristics and evolution of the axial zone on fast spreading mid-ocean ridges, *J. Geophys. Res., 103,* 9827–9855, 1998.

Fox, C. G., W. W. Chadwick Jr., and R. W. Embley, Detection of changes in ridge-crest morphology using repeated

multibeam sonar surveys, *J. Geophys. Res., 97,* 11,149–11,162, 1992.

Fox, C. G., W. E. Radford, R. P. Dziak, T. K. Lau, H. Matsumoto, and A. E. Schreiner, Acoustic detection of a seafloor spreading episode on the Juan de Fuca Ridge using military hydrophone arrays, *Geophys. Res. Lett., 22,* 131–134, 1995.

Gilbert, L. A., and H. P. Johnson, Direct measurements of oceanic crustal density at the northern Juan de Fuca Ridge, *Geophys. Res. Lett., 26,* 3633–3636, 1999.

Gregg, T. K. P., and W. W. Chadwick Jr., Submarine lava-flow inflation: A model for the formation of lava pillars, *Geology, 24,* 981–984, 1996.

Gregg, T. K. P., and J. H. Fink, Quantification of submarine lava-flow morphology through analog experiments, *Geology, 23,* 73–76, 1995.

Gregg, T. K. P., and D. J. Fornari, Long submarine lava flows: Observations and results from numerical modeling, *J. Geophys. Res., 103,* 27,517–27,532, 1998.

Griffiths, R. W., and J. H. Fink, Solidification and morphology of submarine lavas: A dependence on extrusion rate, *J. Geophys. Res., 97,* 19,729–19,737, 1992.

Guest, J. E., C. Wood, and R. Greeley, Lava tubes, terraces and megatumuli on the 1614-24 pahoehoe lava flow field, Mount Etna, Sicily, *Bull. Volcanol., 47,* 635–648, 1984.

Head, J. W., L. Wilson, and D. K. Smith, Mid-ocean ridge eruptive vents: Evidence for dike widths, eruption rates, and evolution of eruptions from morphology and structure, *J. Geophys. Res., 101,* 28,265–28,280, 1996.

Holcomb, R. T., E. Kappel, and S. Ross, Dive report: *Alvin* dive 1461, September 28, 1984, Plume Site, southern Juan de Fuca Rift, *U.S. Geol. Surv. Open File Rep., 86-560-H,* 1–101, 1987.

Holden, J. F., B. C. Crump, M. Summit, and J. A. Baross, Microbial blooms at the CoAxial segment, Juan de Fuca Ridge deep-sea hydrothermal vent site following a magma intrusion, *Eos Trans. AGU, 76*(43), Fall Meet. Suppl., F411, 1995.

Holden, J. F., M. Summit, and J. A. Baross, Thermophilic and hyperthermophilic microorganisms in 3–30°C hydrothermal fluids following a deep-sea volcanic eruption, *FEMS Microb. Ecol., 25,* 33–41, 1998.

Hon, K., J. Kauahikaua, R. Denlinger, and K. Mackay, Emplacement and inflation of pahoehoe sheet flows: Observations and measurements of active lava flows on Kilauea volcano, Hawaii, *Geol. Soc. Am. Bull., 106,* 351–370, 1994.

Johnson, H. P., and M. Hutnak, Conductive heat loss in recent eruptions at mid-ocean ridges, *Geophys. Res. Lett., 24,* 3089–3092, 1997.

Juniper, S. K., P. Martineu, J. Sarrazin, and Y. Gélinas, Microbial-mineral floc associated with nascent hydrothermal activity on CoAxial segment, Juan de Fuca Ridge, *Geophys. Res. Lett., 22,* 179–182, 1995.

Kappel, E. S., and W. R. Normark, Morphometric variability within the axial zone of the southern Juan de Fuca Ridge: Interpretation from SeaMARC II, SeaMARC I, and deep sea photography, *J. Geophys. Res., 92,* 11,291–11,302, 1987.

King, J. S., Selected volcanic features of the south-central Snake River Plain, Idaho, in *Cenozoic Geology of Idaho,* edited by B. Bonnichsen, and R. M. Breckenridge, *Idaho Bur. Mines Geol. Bull., 26,* 439–451, 1982.

Koski, R., and I. Jonasson, Sulfide deposits at the north Cleft segment: implications for the evolution of the hydrothermal system, *J. Geophys. Res., 99,* 4813–4832, 1994.

Kurras, G. J., M. H. Edwards, and D. J. Fornari, High-resolution bathymetry of the East Pacific Rise axial summit trough 9° 49′–51′N: A compilation of *Alvin* scanning sonar and altimetry data from 1991–1995, *Geophys. Res. Lett., 25,* 1209–1212, 1998.

Lerner, S., D. Yoerger, and T. Crook, Navigation for the Derbyshire phase2 survey, *Rep. WHOI-99-11,* 27 pp., Woods Hole Oceanogr. Inst., Woods Hole, Mass., 1999.

Moore, J. G., Mechanism of formation of pillow lava, *Am. Sci., 63,* 269–277, 1975.

Normark, W. R., J. L. Morton, R. A. Koski, D. A. Clague, and J. R. Delaney, Active hydrothermal vents and sulfide deposits on the southern Juan de Fuca Ridge, *Geology, 11,* 158–163, 1983.

Normark, W. R., et al., Submarine fissure eruptions and hydrothermal vents on the southern Juan de Fuca Ridge: Preliminary observations from the submersible *Alvin, Geology, 14,* 823–827, 1986.

Normark, W. R., J. L. Morton, and S. L. Ross, Submersible observations along the southern Juan de Fuca Ridge: 1984 *Alvin* program, *J. Geophys. Res., 92,* 11,283–11,290, 1987.

Perfit, M. R., and W. W. Chadwick Jr., Magmatism at mid-ocean ridges: Constraints from volcanological and geochemical investigations, in *Faulting and Magmatism at Mid-ocean Ridges, Geophys. Monogr. Ser.,* vol. 106, edited by W. R. Buck et al., pp. 59–116, AGU, Washington, D. C., 1998.

Pruis, M. J., and H. P. Johnson, Porosity of very young oceanic crust from seafloor gravity measurements, *Geophys. Res. Lett., 25,* 1959–1962, 1998.

Richter, D. H., J. P. Eaton, K. J. Murata, W. U. Ault, and H. L. Krivoy, Chronological narrative of the 1959–1960 eruption of Kilauea Volcano, Hawaii, *U.S. Geol. Surv. Prof. Pap., 537-E,* 73 pp., 1970.

Rossi, M. J., and A. Gudmundsson, The morphology and formation of flow-lobe tumuli on Icelandic shield volcanoes, *J. Volcanol. Geotherm. Res., 72,* 291–308, 1996.

Rubin, A. M., Dike-induced faulting and graben subsidence in volcanic rift zones, *J. Geophys. Res., 97,* 1839–1858, 1992.

Ryan, W. B. F., M. H. Cormier, A. M. Bradley, D. R. Yoerger, and H. Singh, Branching and confluence of axially-fed lava channels on the crest of the East Pacific Rise at 17°28′S, *Eos Trans. AGU, 80*(46), Fall Meet. Suppl., F1074, 1999.

Scheirer, D. S., D. J. Fornari, S. E. Humphris, and S. Lerner, High-resolution seafloor mapping using the DSL-120 sonar system: Quantitative assessment of sidescan and phase-bathymetry data from the Lucky Strike segment of the Mid-Atlantic Ridge, *Mar. Geophys. Res., 21,* 121–142, 2000.

Singh, H., L. Whitcomb, D. Yoerger, and O. Pizarro, Microbathymetric mapping from underwater vehicles in the deep ocean, *Computer Vision and Image Understanding, 79,* 143–161, 2000.

Smith, D. K., and J. R. Cann, Constructing the upper crust of the Mid-Atlantic Ridge: A reinterpretation based on the Puna Ridge, Kilauea Volcano, *J. Geophys. Res., 104,* 25,379–25,399, 1999.

Smith, D. K., et al., Mid-Atlantic Ridge volcanism from deep-towed side-scan sonar images, 25°–29°N, *J. Volcanol. Geotherm. Res., 67,* 233–262, 1995.

Swanson, D. A., W. A. Duffield, D. B. Jackson, and D. W. Peterson, Chronological narrative of the 1969–71 Mauna Ulu eruption of Kilauea Volcano, Hawaii, *U.S. Geol. Surv. Prof. Pap., 1056,* 55 pp., 1979.

Tivey, M. A., and H. P. Johnson, *Alvin* magnetic survey of zero-age crust: CoAxial segment eruption, Juan de Fuca Ridge 1993, *Geophys. Res. Lett., 22,* 171–174, 1995.

Tivey, M. A., H. P. Johnson, A. Bradley, and D. Yoerger, Thickness measurements of submarine lava flows deter-

mined from autonomous near-bottom magnetic field mapping, *Geophys. Res. Lett., 25,* 805–808, 1997.

Tunnicliffe, V., R. W. Embley, J. F. Holden, D. A. Butterfield, G. J. Massoth, and S. K. Juniper, Biological colonization of new hydrothermal vents following an eruption on Juan de Fuca Ridge, *Deep Sea Res., Part II, 44,* 1627–1644, 1997.

Walker, G. P. L., Structure, and origin by injection of lava under surface crust, of tumuli, "lava rises", "lava-rise pits", and "lava-inflation clefts" in Hawaii, *Bull. Volcanol., 53,* 546–558, 1991.

Wentworth, C. K., and G. A. Macdonald, Structures and forms of basaltic rocks in Hawaii, *U.S. Geol. Surv. Bull., 994,* 95 pp., 1953.

Wessel, P., and W. H. F. Smith, Free software helps map and display data, *Eos Trans. AGU, 72,* 441, 445–446, 1991.

Wolfe, E. W., C. A. Neal, N. G. Banks, and T. J. Duggan, Geologic observations and chronology of eruptive events, in *The Pu'u 'O'o Eruption of Kilauea Volcano, Hawaii: Episodes 1 Through 20, January 3, 1983, Through June 8, 1984,* edited by E. W. Wolfe, *U.S. Geol. Surv. Prof. Pap., 1463,* 1–98, 1988.

W. W. Chadwick Jr. and R. W. Embley, Hatfield Marine Science Center, NOAA/PMEL, 2115 SE OSU Dr., Newport, OR 97365-5258. (chadwick@pmel.noaa.gov; embley@pmel.noaa.gov)

H. P. Johnson, School of Oceanography, University of Washington, Seattle, WA 98195. (johnson@ocean.washington.edu)

D. S. Scheirer, Department of Geological Sciences, Brown University, Providence, RI 02912. (scheirer@emma.geo.brown.edu)

(Received June 16, 2000; revised December 6, 2000; accepted April 12, 2001.)